Highlights

Ion density and phase space density distribution of planetary ions Na$^+$, O$^+$ and He$^+$ in Mercury's magnetosphere

A. L. E. Werner,S. Aizawa,F. Leblanc,J. Y. Chaufray,R. Modolo,J. M. Raines,W. Exner,U. Motschmann,C. Schmidt

- MESSENGER FIPS ion density observation from the whole orbital phase are analyzed.

- Spatial distribution of Na$^+$, O$^+$ and He$^+$ ion densities are reproduced by our model.

- Simulated Na$^+$ and He$^+$ ion densities are overestimated by a factor of 2-20.

- Upstream conditions vary planetary ion densities by almost an order of magnitude.

- Analysis of the ion velocities reveal an anisotropic distribution in the $v_x - v_z$ plane.

Ion density and phase space density distribution of planetary ions Na$^+$, O$^+$ and He$^+$ in Mercury's magnetosphere

A. L. E. Werner[a,*], S. Aizawa[b], F. Leblanc[a], J. Y. Chaufray[c], R. Modolo[c], J. M. Raines[d], W. Exner[e,f], U. Motschmann[f,g] and C. Schmidt[h]

[a]*LATMOS/IPSL, Sorbonne Université, UVSQ, CNRS, Paris, France*
[b]*IRAP, Toulouse, France*
[c]*LATMOS/IPSL, UVSQ Université Paris–Saclay, Sorbonne Université, CNRS, Guyancourt, France*
[d]*Department of Climate and Space Sciences and Engineering, University of Michigan, Ann Arbor, MI, USA*
[e]*Institute for Geophysics and extraterrestrial Physics, TU Braunschweig, Braunschweig, Germany*
[f]*Institute for Theoretical Physics, TU Braunschweig, Braunschweig, Germany*
[g]*DLR Institute of Planetary Research, Berlin, Germany*
[h]*Center for Space Physics, Boston University, USA*

ARTICLE INFO

ABSTRACT

Photo-ionization of Mercury's tenuous exosphere contributes to the heavy ion population in the Hermean environment. Observations with the MESSENGER Fast Imaging Plasma Spectrometer (FIPS) have revealed the ion density and spatial distribution of the three most abundant planetary ions or ion groups around Mercury: The Na$^+$-group (mass-per-charge ratio m/q = 21 − 30 amu/e), O$^+$-group (m/q = 16 − 20 amu/e) and He$^+$. We developed a test-particle model coupled to a neutral exosphere model and two different models of the magnetosphere to simulate the ion density distribution of Na$^+$, He$^+$ and O$^+$. We compare the modeled ion density distribution at aphelion for northward interplanetary magnetic field (IMF) with FIPS observations from the entire orbital phase (23 March 2011 to 30 April 2015). Our model reproduces several observed features but the average ion density is up to 18x too high. However, we find that the discrepancy is less than 3x for other solar wind and exosphere conditions. Comparison with previous simulation studies of the Na$^+$ ion density and magnetic field line resonance observations give an average Na$^+$ density which is on the same order as our estimate. Finally, we model the phase space density (PSD) distribution in four different regions. We find that in three out of four regions only a fraction of the PSD distribution can typically be observed by FIPS. This is mainly due the obstruction of the field-of-view caused by the spacecraft's sun shield, which blocks plasma with a high v_x/v_z ratio from entering the instrument.

1. Introduction

Mercury has a tenuous and nearly collisionless atmosphere (exosphere) that is rich in heavy elements. H, He, Na, K, Mg, Ca, Mn, Fe and Al have been detected through ground-based (Potter and Morgan, 1985, 1986; Bida et al., 2000; Doressoundiram et al., 2009; Bida and Killen, 2017) and in-situ observations (Broadfoot et al., 1976; McClintock et al., 2008; Vervack et al., 2016). Space probe Mariner 10 made a tentative detection of the 130.4 nm O emission line during its third flyby past Mercury (Hunten et al., 1988). O could not be observed by the more recent Mercury Surface, Space Environment, Geochemistry, and Ranging (MESSENGER) spacecraft, despite conducting regular observations of the 130 nm line for several years in orbit (Vervack et al., 2016).

The strong solar radiation at Mercury and the intense space weathering causes neutral species to be continuously released from the surface regolith, either thermally (thermal desorption), by individual photons exciting the surface-bound atoms (photo-stimulated desorption), sputtering by solar wind ions or vaporization of whole surface grains by micro-meteoroids. The relative importance of these ejection mechanisms vary depending on species, and is different between volatile species (Na,K,He) and refractory species (Mg, Ca). Because the exosphere is collisionless, the species are not coupled and have their own dynamics. Several models have been developed to determine the relative contribution of the different ejection and loss processes to the overall composition of Mercury's exosphere (Smyth

59 and Marconi, 1995; Killen et al., 2001; Wurz and Lammer, 2003; Leblanc and Johnson, 2003, 2010; Schmidt, 2013;
60 Gamborino et al., 2019).

61   Mercury has a highly eccentric orbit ($\epsilon = 0.2056$) and is trapped in a 3:2 spin-orbit resonance with the Sun. This
62 gives rise to cold and hot longitudes (Soter and Ulrichs, 1967) and a seasonally variable exosphere and sodium ion
63 content (Cassidy et al., 2015, 2016; Jasinski et al., 2021). Some exospheric sources like micro-meteoroid vaporization
64 (Janches et al., 2021) and ion sputtering vary on shorter timescales, which has an impact on both the neutral exosphere
65 (Leblanc et al., 2009; Orsini et al., 2018) and ionized exospheric neutrals (Raines et al., 2018; Jasinski et al., 2020).
66 Meteoroids (as opposed to micrometeoroids) have been detected as large, brief enhancements to the exosphere (Jasinski
67 et al., 2020; Cassidy et al., 2021)

68   The strong solar radiation at Mercury produces a large flux of heavy ions (on the order of 10^{24} s^{-1}; Raines et al.,
69 2015) from the ionization of the exosphere. Lesser sources of planetary ions include charge exchange and solar wind
70 ion sputtering. MESSENGER Fast Imaging Plasma Spectrometer (FIPS) detected several mass spectrum peaks that
71 may belong to Na$^+$ (mass-per-charge ratio m/q = 23-24 amu/e), O$^+$ and water group ions (16-18 amu/e), S$^+$ and H$_2$S$^+$
72 (32-36 amu/e), Si$^+$ (28 amu/e), K$^+$ and Ca$^+$ (39-40 amu/e) and He$^+$ (4 amu/e; Zurbuchen et al., 2008). FIPS is a
73 time-of-flight (TOF) mass spectrometer. Due to FIPS TOF uncertainty, ions with similar mass-per-charge ratio were
74 grouped together in so-called ion groups (e.g. Appendix A in Raines et al., 2013). Na$^+$- (m/q = 21-30 amu/e), O$^+$-
75 group (m/q = 16-20 amu/e) ions and He$^+$ (m/q = 4 amu/e) were regularly observed during the mission orbital phase
76 (Zurbuchen et al., 2011; Raines et al., 2013). Ca$^+$ has also been detected by the Mercury Atmospheric and Surface
77 Composition Spectrometer (MASCS) UltraViolet and Visible Spectrometer (UVVS; Vervack et al., 2016).

78   Observations with the magnetometer (MAG) on MESSENGER have shown that Mercury possesses a weak intrinsic
79 magnetic field that fits the profile of a axially symmetric dipole field with dipole magnetic moment of 195 ± 10 nT-R$_M^3$
80 (where R$_M$ = 2440 km is the mean Mercury radius) and a 0.2 R$_M$ northward offset (Anderson et al., 2011). The planet
81 takes up a relatively large volume inside the magnetosphere, and the magnetopause standoff distance is typically located
82 at a mere 0.45 R$_M$ from the subsolar point on the surface (Winslow et al., 2013). Despite the weak dipole magnetic
83 moment and the high solar wind ram pressure, the dayside magnetosphere is rarely compressed all the way to the
84 surface (Slavin et al., 2019; Winslow et al., 2020). This is due to the existence of induction currents in Mercury's
85 interior that are driven by solar wind variations (Smith et al., 2012; Slavin et al., 2014; Jia et al., 2015). The Hermean
86 magnetosphere is highly dynamic with a Dungey cycle (Dungey, 1961) time of approximately 2 minutes (Slavin et al.,
87 2009). The same process typically takes 1 hour at Earth (Siscoe et al., 1975).

88   The comparatively large gyro radius of the heavy ions in relation to the small scale of the Hermean magnetosphere
89 means that non-adiabatic effects are significant almost everywhere in the magnetosphere (Delcourt et al., 2003). Non-
90 adiabatic effects include centrifugal ion acceleration (Delcourt et al., 2002, 2003), which may have a major impact on
91 the ion distribution in the magnetosphere (Raines et al., 2013). The heavy ion population is likely not dense enough to
92 influence the global structure of the Hermean magnetosphere (Exner et al., 2020) but it gives rise to other effects like
93 diamagnetic depression of the magnetic field (Korth et al., 2011), enhancement of the formation of Kelvin-Helmholtz
94 instabilities (Paral et al., 2010) and generation of magnetic field-line-resonances (James et al., 2019).

95   Analysis of the first few months of FIPS observations in orbit around Mercury revealed several ion density en-
96 hancement regions and surprising differences between He$^+$ and the heavier O$^+$- and Na$^+$-group ions. The Na$^+$- and
97 O$^+$-group ions were especially abundant near the northern magnetic cusp with a Na$^+$-group ion abundance four time
98 larger than the solar wind He^{++}. The elliptical polar orbit of MESSENGER did not permit observations at low alti-
99 tudes in the southern polar region. A later study by Raines et al. (2014) identified two populations of Na$^+$-group ions
100 in the northern cusp: one at low energy (100 – 300 eV) and one at high energy (> 1000 eV). The low-energy ions
101 are believed to be produced locally while the high-energy ions come from photo-ionized escaping neutrals that have
102 been swept into the magnetic cusps by reconnection. The Na$^+$- and O$^+$-group ions also showed smaller enhancements
103 near the dawn terminator in the equatorial plane and at high altitudes (> 2000 km) in the dusk to pre-midnight sector.
104 He$^+$ was much more evenly distributed in the magnetosphere and did not exhibit any particular enhancements in said
105 regions. The density of all species was particularly low near 12 h local time.

106   The Na$^+$ density enhancement near the dawn terminator may be related to the seasonal dawn enhancement in the
107 neutral exosphere (Potter et al., 2006, 2013; Cassidy et al., 2016; Milillo et al., 2021). If this is true, it could imply a
108 direct link between the neutral surface abundance and the ion density at low altitudes. The dusk enhancement, on the
109 other hand, may be evidence of the non-adiabatic ion acceleration mechanism described in Delcourt et al. (2002, 2003).
110 The difference in spatial distribution between He$^+$ and the heavier ion species may imply that He$^+$ is produced by a
111 different, more diffuse source. The depression at the subsolar point may be an apparent effect caused by the effective

energy range (100 eV – 13 keV; Raines et al., 2013).

Raines et al. (2013) also studied the variation of the global average ion density as a function of true anomaly angle. The global averages consist of FIPS data taken at different altitudes, latitudes and local times, and even includes measurements taken inside the solar wind. They found two peaks for the Na$^+$- and O$^+$-group ions, a global maximum at TAA = 110° and local maximum at 330°, and a minimum at TAA = 270°. He$^+$, on the other hand, showed very little variation with TAA. More recently, Jasinski et al. (2021) estimated the TAA variation of the Na$^+$ production rate from UVVS (Cassidy et al., 2015) and THEMIS observations (Milillo et al., 2021) of the Na exosphere and FIPS Na$^+$-group ion observations taken inside the northern magnetospheric cusp. They estimated a maximum ion production rate of $3 - 4 \times 10^{24}$ s^{-1} between TAA = 0° $-$ 30°, where FIPS observations are missing.

In this study, we have modeled planetary ions produced from the exosphere by combining different simulations. In Section 2, we describe the models used in this study. In Section 3 we describe the modeled neutral exosphere, magnetic and electric fields in the magnetosphere and the solar wind proton density. Then, we compare the modeled ion density and phase space density distribution with FIPS observations. We discuss the results and their implications in Section 4 and summarize the main findings in Section 5.

2. Models

In order to study the inferred link between the neutral and ionized exospheres we will use a realistic description of Mercury's neutral exosphere consistent with remote and in-situ observations to model the abundance and spatial distribution of Na$^+$, He$^+$ and O$^+$ in and outside Mercury's magnetosphere. We will account for non-adiabatic effects of the heavy planetary ions and their impact on the ion density distribution by coupling our model to two different hybrid models of the magnetosphere.

In the following subsection, we describe the Monte Carlo-model of the neutral exosphere, the two magnetospheric models and our newly developed test-particle model that computes the full equation of motion of the ions.

2.1. Exospheric Global Model (EGM)

The Exospheric Global Model (EGM; Leblanc et al., 2017b) is a parallelized Monte Carlo-model that describes the exosphere around moons and planets. EGM has been previously used to study the exospheres of Mercury (Leblanc and Johnson, 2003, 2010; Leblanc and Doressoundiram, 2011; Leblanc and Chaufray, 2011; Leblanc et al., 2013), Ganymede (Leblanc et al., 2017b), Mars (Leblanc et al., 2017a) and Europa (Oza et al., 2019). In this paper, we use EGM to simulate the density of Na, He and O in the exosphere of Mercury.

EGM reconstructs the exospheric neutral density, average velocity, kinetic temperature and ionization rate in 3-D as well as the amount of exospheric materials trapped in the surface. The quantities are computed on a spherical grid (r, θ, ϕ) where r is the distance from the planet, θ is the co-latitude and ϕ is the longitude. For Mercury, the grid is centered on the planet ($r = 0$) and extends from the surface ($r = 1$ Mercury radius; R_M) up to 5.5 R_M. The grid is divided into cells that are distributed exponentially with r, linearly spaced in ϕ and defined in θ such that all cells at a given altitude have the same volume. For a detailed description of the EGM parallelization scheme see Turc et al. (2014).

A large number of test-particles are ejected from the surface by different mechanisms (see below) and then continuously throughout the simulation. Each test-particle i represents a large number of actual particles, represented by a weight w_i. Each test-particle is followed around Mercury taking into account the various gravity fields (those of Mercury and the Sun) and the effect of the solar radiation pressure. This is done up to the moment when the test-particle is either ionized by the solar radiation flux (calculated taking into account the relative velocity of the test-particles with respect to the Sun and its distance to the Sun), impact the surface or escape from the simulation. In the case of a surface impact, the particles can be either re-ejected or absorbed in the surface, an absorption which duration is estimated for each species and from the local surface temperature (for a detailed description of the simulation scheme, see Leblanc and Johnson, 2010; Leblanc et al., 2017b). The surface temperature is described using a one-dimensional heat conduction model (see Leblanc et al., 2017b). An EGM run last for several Mercury years in order to reach an orbital dependent stationary solution independent from the initial conditions. Once a stationary solution has been reached, the state of the exosphere can be determined at any point along the orbit. To improve the statistics, the 3D density (velocity, ionization rate etc.) at a given TAA is averaged over 20° centered on the TAA in question.

In the following, we assume that the primary origin of the exospheric Na and O atoms is Mercury's surface, either endogenic (internal by regolith diffusion) or exogenic (meteorite origin), while He is primarily coming from implanted

Table 1
Input parameters to the EGM model.

Parameter:	Value:		
Species:	Na	O	He
Ejection processes and surface ejection rate [s⁻¹]:	3.4×10^{25} (PSD) 1.7×10^{23} (MMV) 1.9×10^{23} (SWS)	3.7×10^{22}	5.9×10^{23}
Ionization frequency (at 1 AU in s⁻¹):	5.0×10^{-6}	3.1×10^{-7}	7.5×10^{-8}
Time step:	$\Delta t = 0.81$ s		
Number of cells:	$nr = 80,$ $n\theta = 18$ $n\phi = 40$		
Simulation domain:	$1.0 < r < 5.5\ R_\mathrm{M}$ $0 < \phi < \pi$ rad $0 < \phi < 2\pi$ rad		
Grid resolution:	$\Delta r = 5\text{-}287$ km $\Delta\phi = \frac{\pi}{2}$ rad $\Delta\theta = \frac{\pi}{3} - \frac{\pi}{6}$ rad		
True anomaly angle (TAA):	180°		

solar wind alpha particles. Na and O are launched from the entire surface of Mercury by various ejection mechanisms so that their ejection rate is non uniform, while He is launched from the magnetic cusp regions where solar wind alpha particles can reach the surface. The input parameters to the EGM simulations are listed in Table 1.

2.1.1. Na

We use the same approach as described in Leblanc and Johnson (2010) to model the Na exosphere. Micro-meteoroid impact vaporization (MMV) is described as a source of Na atoms of 5×10^5 Na cm² s⁻¹ ejected with a Maxwellian-Boltzmann (MB) distribution with a temperature of 3000 K. Photon-stimulated desorption (PSD) is described following a Maxwellian-Boltzmann flux (MBF) distribution with a temperature of 1500 K and an ejection rate determined from a cross-section of 0.68×10^{-17} cm² and a dependency with the surface temperature as in Schmidt (2013) using an activation energy set to 0.02 eV. Thermal desorption (TD) is described by a MBF distribution with binding energy between 3.5-4.5 eV and vibrational frequency 2.5×10^{10} s⁻¹. Solar wind ion sputtering (SWS) is described using a yield of 0.15 that is reduced by a factor 2 due to the porosity, a typical solar wind flux corresponding to a velocity of 400 km/s, a density of 10 cm⁻³ and an increase by a factor 4 due to the cusps geometry (defined in Leblanc and Johnson, 2010). The energy distribution of the sputtered Na atoms follows a distribution at $f(E) = UE/(E + U)^3$ with the binding energy U set to 0.27 eV (Leblanc and Johnson, 2003). The ejection rate of each of these processes depends on the Na surface concentration and also on the relative efficiency of each of them (see Leblanc and Johnson, 2003, 2010, for more details and discussions). Column density profiles of the model Na exosphere roughly agrees in both shape and magnitude with UVVS limb scan taken at the south pole and at different local times near the equator (see Figure 4 in Cassidy et al., 2015).

We consider photo-ionization as the main source of the planetary ion population and neglect electron impact ionization as well as ion production caused by solar wind ion sputtering or micro-meteoroid impact vaporization.

Na photo-ionization rate, g-value and radiation pressure are computed as in Leblanc and Johnson (2010), consistent with cometary Na tail observations in the inner heliosphere (Fulle et al., 2007). The calculated Na photo-ionization
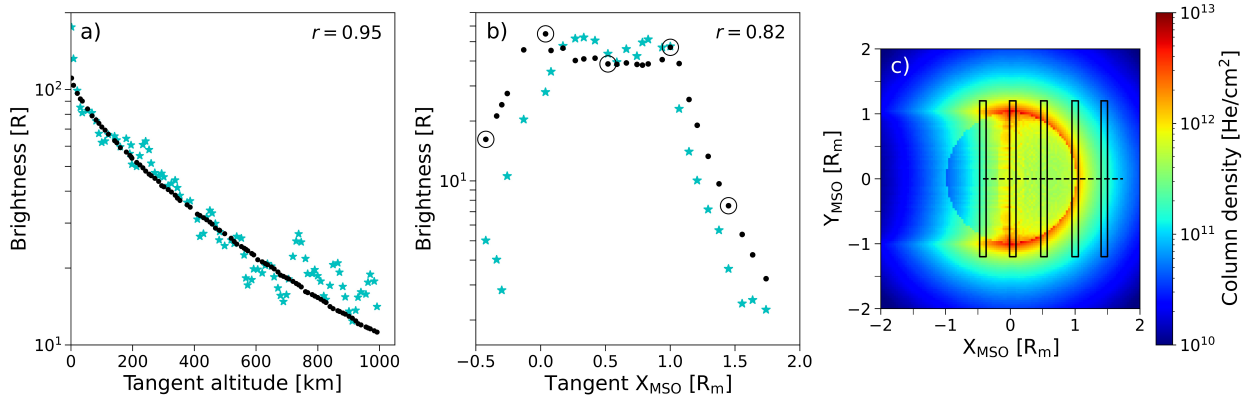
Figure 1: The fit between EGM (black line) and the Mariner 10 He column density observations (green stars) at (a) the subsolar limb and (b) the terminator. Also shown is the (c) simulated 2-D column density map in the equatorial plane and the approximate viewing geometry of Mariner 10 during the terminator observations. The boxes in (c) represent the approximate slit size of the observations. The circled points in (b) show the X_{MSO} coordinates of the boxes in (c). The correlation values r between the best-fit model and the two sets of observations are written in the top right corner of (a) and (b).

185   rate (5.0×10^{-6} s^{-1} at 1 AU) is close to the value published in Fulle et al. (2007).

2.1.2. He

187   Following Leblanc and Chaufray (2011), we consider He atoms ejected thermally from the surface. In the version
188 of EGM used by Leblanc and Chaufray (2011) the ejection rate of He was set to 2.3×10^{23} s^{-1} in order to reproduce
189 the Mariner 10 column density profiles of the 58.4 nm He emission line. Leblanc and Chaufray (2011) defined the
190 He source area to the whole surface of Mercury but in this work we limit the He source to the magnetospheric cusps.
191 This is likely more realistic considering that the solar wind bombardment is limited to the cusps during nominal solar
192 wind conditions. We define the location and size of the northern cusp as $27° - 54°$ in latitude (where $0°$ is the north
193 pole and $90°$ is the equator) and 10 - 14 h in local time. We define the southern cusp symmetrically in the southern
194 hemisphere. The northern cusp area defined here compares well to the limits of the northern cusp inferred from MAG
195 data (Winslow et al., 2012), although the mean latitudinal extent ($11°$) of the northern cusp is smaller.
196   We find that we have to increase the He ejection rate to 5.9×10^{23} s^{-1} to fit the Mariner 10 column density profiles
197 in 1. This is still much smaller than the He^{++} flux during nominal solar wind conditions (Leblanc and Chaufray, 2011).
198 The fit of the new model to the Mariner 10 observations (5.9×10^{23} s^{-1}) gives similar correlation factors to Leblanc
199 and Chaufray (2011), but the fit to the terminator observations is slightly worse ($r = 0.82$ compared to $r = 0.93$ from
200 Leblanc and Chaufray, 2011). In Leblanc and Chaufray (2011) the energy accommodation of the He atoms follow a
201 linear relationship between full accommodation on the dayside ($\alpha = 1$) to weak accommodation with the surface on
202 the nightside ($\alpha = 0.06$ at the terminator and $\alpha = 0.05$ at midnight). The new fit in Figure 1b may imply that the
203 accommodation theory developed for neutral He in Leblanc and Chaufray (2011) may need to be tweaked to better fit
204 this set of observations. Since our study mainly concerns the ion density distribution near the equatorial plane, where
205 the fit to the neutral He observations is good (Figure 1a; $r = 0.95$), we expect that this will have negligible impact on
206 our results. Neutral He could not be observed by MESSENGER due to the limited coverage of the UVVS instrument
207 in the ultraviolet spectral range (McClintock and Lankton, 2007).
208   The ionization frequency calculation follows the same scheme used for Na and is estimated to 0.1×10^{-6} s^{-1} for He
209 at 1 AU. The solar radiation pressure is also calculated as in Fulle et al. (2007), but for both He and O it is negligible
210 with respect to Mercury's gravity field.

2.1.3. O

212   As explained in the introduction, the oxygen density in the exosphere of Mercury is not well constrained by obser-
213 vations, only an upper limit could be derived from UVVS observations (Vervack et al., 2016). Moreover, how oxygen
214 could be ejected from the surface into the exosphere is not known. Therefore, due to this lack of observations, oxygen

Table 2
Input parameters to LatHyS and AIKEF.

Parameter:	Lathys value:	AIKEF value:
Time step:	0.02 s	0.01 s
Spatial resolution:	145 km	100 km
Simulation domain:	$-5.4 < x < 5.6$ R$_M$ $-11.3 < y < 11.4$ R$_M$ $-11.3 < z < 11.4$ R$_M$	$-3.5 < x < 10.5$ R$_M$ $-5.0 < y < 5.0$ R$_M$ $-5.0 < z < 5.0$ R$_M$
Simulated species:	H$^+$, He^{++}, Na$^+$, H$^+$(planetary)	H$^+$
Number of solar wind particles per cell:	H$^+$: 20 He^{++}: 2	H$^+$: 25
Solar wind number density:	$n = 30$ cm^{-3}	
Solar wind velocity:	$v = 400$ km/s	
Solar wind magnetic field:	$\mathbf{B} = (B_x, B_y, B_z) = (0, 0, +20)$ nT	
Ram pressure:	$P_{ram} = 8$ nPa	
Alfvén Mach number:	$M_A = 5.2$	

exospheric atoms will be simply simulated starting from a population of ejected atoms from the surface following a MBF distribution at the local surface temperature and proportional to the incident solar radiation flux (that is with a dependency in cosine of the solar zenith angle and no ejection from the nightside). For O we assume a uniform weak thermal accommodation with the surface ($\alpha = 0.11$; Hunten et al., 1988). Hence, when a O test-particle impacts the surface it is immediately re-ejected into the exosphere again. We then scale the O exosphere to fit the upper emission limit (≈ 2 Rayleigh) set by UVVS based on observations of the 130.4 nm O emission line (Vervack et al., 2016; Mcclintock et al., 2018). The O ionization rate at 1 AU is 3.1×10^{-7} s^{-1}.

More recently, Huebner and Mukherjee (2015) re-evaluated the photo-ionization cross-sections, rates and excess energies for a range of atomic species, including the species that we consider in this work. The updated photo-ionization cross sections for Na, O and He are not significantly different from ours and we are using a better resolved solar spectrum compared to Huebner and Mukherjee (2015) (which used the same solar spectrum as in Huebner et al., 1992). For this reason there is a factor $1.6 - 3.2$ difference between our calculated photo-ionization rates and the values published in Huebner and Mukherjee (2015). We will only consider quiet solar wind conditions in this work, but it is noteworthy that in the case of both He and O the photo-ionization rate is a factor of $2-3$ higher during high solar activity (Huebner and Mukherjee, 2015). The photo-ionization rate for Na is not nearly as dependent on the solar activity level as O and He (the difference is less than 10 %).

2.2. Models of Mercury's magnetosphere

Both magnetohydrodynamic (MHD; Jia et al., 2015, 2019; Dong et al., 2019) and hybrid (Kallio et al., 2011; Müller et al., 2011; Modolo et al., 2016) models have been employed to describe the electromagnetic field environment around Mercury, which results from the solar wind interaction with Mercury's intrinsic field. Hybrid (electron fluid, ion kinetic) models are particularly well suited to describe plasma processes in systems where the ion Larmor radius is comparable to the length scale of the obstacle itself (Glassmeier et al., 2003; Slavin et al., 2008). Hybrid models have a large computational load compared to MHD models, but they enable higher accuracy in regions where kinetic effects of the ions prevail. We will compare the solar wind H$^+$ and planetary ion densities using static electric and magnetic fields from two such models: Latmos Hybrid Simulation (LatHyS; Modolo et al., 2016) and Adaptive Ion-Kinetic

Table 3
Input parameters to the LIZE model.

Parameter:	Value:
Time step	Adaptive
Number of cells:	$nr = 65$
	$n\theta = 40$
	$n\phi = 60$
Simulation domain:	$r = 1.0 - 3.5\ \mathrm{R_M}$
	$\phi = 0 - 2\pi$ rad
	$\theta = 0 - \pi$ rad
Grid resolution:	$\Delta r = 5 - 600$ km
	$\Delta\phi = 0.08$ rad
	$\Delta\theta = 0.1$ rad
Species:	Na$^+$, O$^+$, He$^+$
Number of test-particles/cell:	$n = 100$
Energy range:	$1 - 10^5$ eV
Energy resolution:	$(E_i - E_{i-1})/E_i = 0.1$, where E_i is the ith energy step

Electron-Fluid (AIKEF; Müller et al., 2011).

We use a single set of solar wind ($n = 30$ cm^{-3}, $v = 400$ km/s) and IMF ($\mathbf{B} = B_z = +20$ nT) boundary conditions (see Table 2). This corresponds to "case a" with $B_z > 0$ described in Aizawa et al. (2021), where B_z is the z-component of the the interplanetary magnetic field (IMF) in the Mercury-Sun Orbital (MSO) system. In MSO coordinates, x points toward the Sun, z points toward the north pole and y completes the right-handed coordinate system (i.e. positive toward dusk).

2.2.1. Latmos Hybrid Simulation (LatHyS)

LatHyS (Modolo et al., 2016) is a hybrid model that describes the 3-D plasma environment around weakly magnetized and unmagnetized planetary bodies. The model has been previously applied to Mercury (Richer et al., 2012), Mars (Modolo et al., 2016; Romanelli et al., 2018a,b), Ganymede (Leclercq et al., 2016) and Titan (Modolo et al., 2007). See Modolo et al. (2016) for further details on LatHyS.

The spatial and temporal resolution used in the LatHyS simulation are $\Delta x = 145$ km and $\Delta t = 0.02$ s. Two solar wind ion (H$^+$ and He^{++}) and two planetary ion (Na$^+$ and H$^+$) species are considered in the simulation. The Na$^+$ (H$^+$) ion density distribution in LatHyS is derived from a simple homogeneous Na (H) density model with a surface number density of 10^5/cm^3 (10^4/cm^3) and a scale height of 50 km (1292 km). Macro-particles from the planetary ion distribution are added directly to the total particle count of the simulation.

2.2.2. Adaptive Ion-Kinetic Electron-Fluid (AIKEF)

AIKEF is another hybrid model which has also been used to describe the interaction between magnetized plasma and different types of obstacles, such as planets, moons and comets (Müller et al., 2011). AIKEF has been employed in the past to study Mercury's apparent double magnetopause (Müller et al., 2012), the impact of a temporally variable coronal mass ejection on Mercury's magnetosphere (Exner et al., 2018) and the influence of exospheric Na$^+$ on the magnetic and electric fields inside Mercury's magnetosphere (Exner et al., 2020).

The AIKEF simulation employs a grid size defined by $\Delta x = 100$ km, a time step $\Delta t = 0.01$ s and a larger number of macro-particles compared to LatHyS (see Table 2). This means that the AIKEF solution have better statistics compared to LatHyS. We only consider solar wind and planetary H$^+$ in this AIKEF simulation. AIKEF uses so called "ghost

265 particles" with negligible density to fill vacuum regions above Mercury's nightside surface.

2.2.3. *Latmos IoniZed Exosphere (LIZE)*

267 Even with current high-perfomance computing, it is still not possible to simulate directly the three ion populations
268 in the two hybrid models with good statistics. The global structure of Mercury's magnetosphere is not altered signifi-
269 cantly by a tenuous sodium exosphere (Exner et al., 2020). Therefore, a valid method to reconstruct the planetary ion
270 density with sufficient statistics under stationary upstream conditions, is to employ a test-particle model with a static
271 electromagnetic environment.

272 The Latmos IoniZed Exosphere (LIZE) model is a test-particle model that describes the ion density of planetary
273 ions in the magnetosphere of Mercury. The planetary ion populations are produced by photo-ionization of exospheric
274 neutrals. We use the simulated ion production rate from EGM to define the statistical weights of the test-particles. The
275 full equation of motion of the test-particles is then computed using a Fourth-order Runge-Kutta scheme employing the
276 electromagnetic fields calculated from LatHyS or AIKEF.

277 The test-ions are injected in the whole 3-D volume and then tracked until they leave the simulation box, impact
278 the surface or exceed a postulated maximum iteration count. 100 test-particles are launched in each cell with zero
279 initial velocity. We find that a non-zero injection velocity that is comparable to the average velocity distribution of the
280 neutrals does not change the results. We use a static spatial grid but an adaptive time step that is limited by the gyro
281 radius and the size of the LatHyS (or AIKEF) spatial grid. We use a spherical coordinate system that is logarithmic in
282 r and uniform in both co-latitude θ and longitude ϕ (see Table 3).
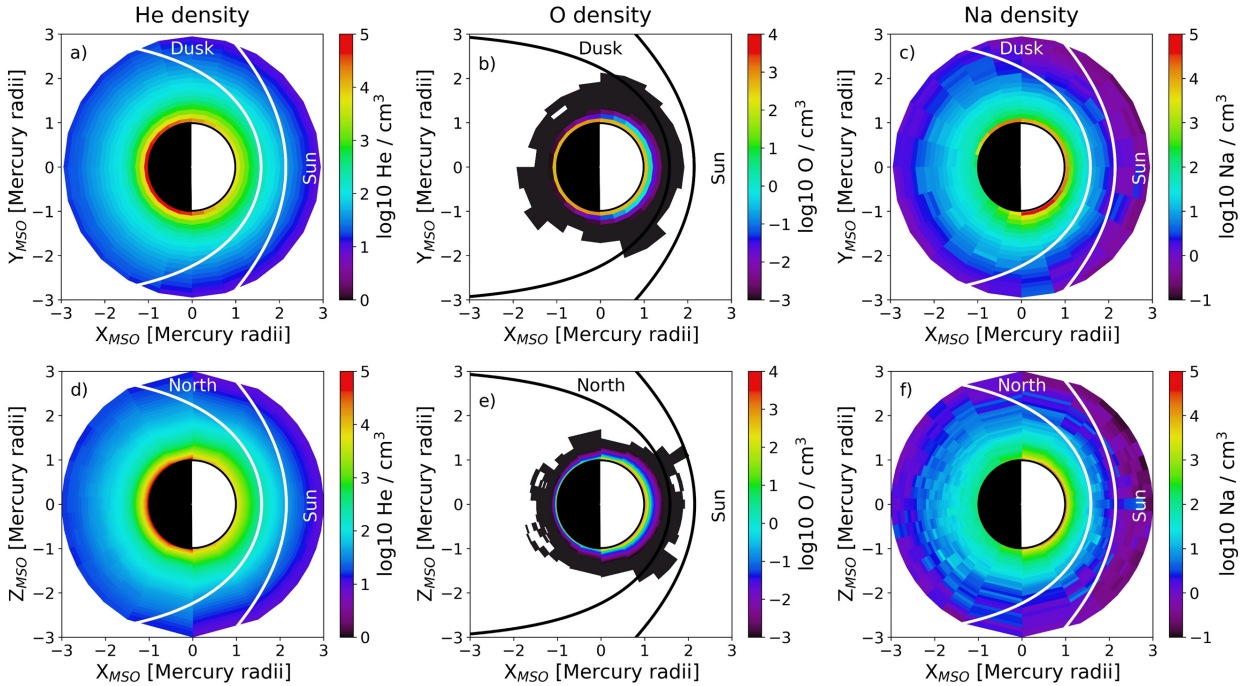

Figure 2: The neutral He, O and Na density computed with EGM, here shown in the equatorial (top row) and the noon-midnight meridional plane (bottom row). The curved lines show the location of the magnetopause and bow shock boundaries (Winslow et al., 2013).

3. Results

3.1. Neutral density

285 Figure 2 shows the simulated neutral He, O and Na density at aphelion from the EGM in the MSO XY plane (top
286 row) and the MSO XZ plane (bottom row). The neutral density was averaged between $TAA = 170 - 190°$ to give an
287 accurate description of the exosphere at aphelion (TAA = 180°). At this point in the orbit the average neutral density

typically reaches its maximum value (Cassidy et al., 2015) and the photo-ionization rate its minimum value. Rather than averaging the neutral density over all possible TAAs with the EGM, computing the ion density at aphelion may be sufficient to give us a broad idea of the average ion density that we can expect over the whole Mercury orbit. The neutral density in the XY (XZ) plane was averaged over a volume segment spanning $\pm 10°$ in latitude (longitude). The He and Na exospheres are seen to extend well beyond the magnetospheric boundaries while the O exosphere concentrated to low altitudes (see Figure 2).

The location of the magnetopause boundary in Figure 2 was calculated from the Shue et al. (1997) model described in Winslow et al. (2013) that has been fitted to MESSENGER MAG data and then corrected for the solar wind ram pressure of our simulation ($P_{ram} = 8$ nPa; Table 2). The bow shock location was then determined from the Slavin et al. (2007) model and corrected for the solar wind Alfvén Mach number ($M_a = 5.2$; Table 2) following the scaling method proposed by Winslow et al. (2013).

The He exosphere is characterized by a higher density on the nightside (see Figure 2a and 2d), which is in agreement with Mariner 10 observations (Broadfoot et al., 1976). The maximum He density is 6.3×10^4 cm^{-3} at the midnight surface. The total He supply rate (5.9×10^{23} s^{-1}) is balanced by 32 % thermal escape (1.9×10^{23} s^{-1}) and 68 % loss by photo-ionization (4.0×10^{23} s^{-1}).

The simulated O ejection rate 3.7×10^{22} s^{-1} was fitted to the upper limit on the average O tangent column density between 0-500 km above the subsolar point (2.0×10^{10}/cm^2; Mcclintock et al., 2018) inferred from UVVS observations (Vervack et al., 2016). The O density is highest at noon (9.9×10^2 cm^{-3}). The total O supply rate (3.7×10^{22} s^{-1}) corresponds to 64 % loss by photo-ionization (2.4×10^{22} s^{-1}) and 36 % thermal escape (1.3×10^{22} s^{-1}). We did not study the seasonal variability of the global O ion production rate with EGM.

The Na surface density is lowest on the nightside (9.2×10^1 cm^{-3} at the surface), has a local maximum at the dusk terminator (1.7×10^4 cm^{-3}) and a global maximum at the dawn terminator (5.9×10^4 cm^{-3}). Between TAA $= 170 - 190°$, the Na exosphere is mainly supplied by photo-desorption (3.4×10^{25} s^{-1}) and to a much lesser degree by micro-meteoroid vaporization (1.7×10^{23} s^{-1}) and solar wind ion sputtering (1.9×10^{23} s^{-1}). Thermal desorption is negligible with respect to the other ejection processes at aphelion. The global Na supply rate (3.5×10^{25} s^{-1}) is balanced by 37% loss by photo-ionization (1.3×10^{25} s^{-1}) and 63% thermal escape (2.2×10^{25} s^{-1}). When we compare the global Na$^+$ ion production rate at different TAA, we find that the maximum photo-ionization loss rate of neutral Na occurs during aphelion (1.3×10^{25} s^{-1}) and the minimum is located at $TAA = 60°$ (1.5×10^{24} s^{-1}). The Na$^+$ production rate is roughly proportional to the total number of Na atoms in the exosphere (altitude range: 0-2 R$_M$), which also has a maximum at aphelion (3.1×10^{29} atoms) and a minimum at $TAA = 60°$ (1.4×10^{28} atoms) in our model.

The seasonal variation of the global Na$^+$ production rate from our model agrees very well with the Jasinski et al. (2021)'s estimates at perihelion and the first part of Mercury's outbound orbit around the Sun (i.e. 3.0×10^{24} s^{-1} at TAA $= 0°$, 1.5×10^{24} s^{-1} at TAA $= 60°$ and 3.8×10^{24} s^{-1} at TAA $= 120°$). However, during the inbound orbit our model produces much higher values than Jasinski et al. (2021) (i.e. 1.1×10^{25} s^{-1} at TAA $= 240°$ and 5.1×10^{24} s^{-1} at TAA$= 300°$). There is no estimate to compare our model to at TAA$= 180°$ due to the lack of UVVS and THEMIS observations near aphelion.

3.2. Mercury's magnetosphere

Figure 3 shows the solar wind H$^+$ density, the absolute magnetic and electric field ($|B|$, $|E|$), and the H$^+$ plasma bulk velocity (V_{bulk}) in the equatorial plane from LatHyS and AIKEF.

LatHyS and AIKEF yield very similar solar wind H$^+$ density distributions, electromagnetic fields and bulk velocities. The bow shock and magnetopause stand-off distances are smaller for AIKEF. The magnetopause boundary is also more compressed toward the tail for AIKEF (see Figure 3a and 3e). There are a few small regions with high electric field ($|E| \approx 5$ mV/m) relative to the surroundings ($|E| \approx 0$) close to the surface in both models (see Figure 3c and 3d). Test-particle ions which encounter these regions in the LIZE model may be subject to sudden particle acceleration. However, we find that these regions are too small ($\sim 200^3$ km^3) to have a substantial impact on the ion velocities. There exists a rather dense nightside ion ring distribution in the AIKEF simulation. The H$^+$ ions in this region have likely become momentarily trapped in the closed field region of Mercury's intrinsic field and experience a slow azimuthal drift toward the dayside. However, this ion population is unlikely to form a steady ion drift belt due to the small size of the magnetosphere.

In order to check the accuracy of our LIZE model, we simulated the solar wind H$^+$ density distribution with LIZE using the input parameters of the LatHyS and AIKEF simulations (see Table 2) and compared the results to Figure 3a and 3e to validate the simulated density by LIZE. We launched 250,000 test-particles at X=3.4 R$_M$ uniformly
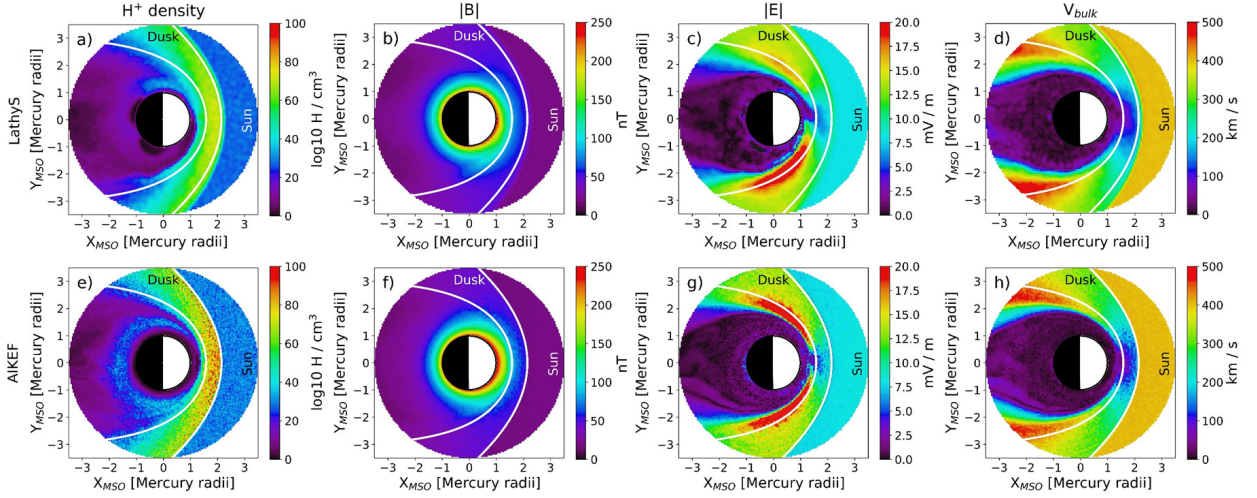
Figure 3: The outputs from two hybrid simulations. (a,e) The solar wind H$^+$ density, (b,f) the total magnetic field, (c,g) the electric field and (d,h) the bulk velocity in the equatorial plane from LatHyS (top row) and AIKEF (bottom row) respectively. The solid white lines in each figure show the location of the magnetopause and bow shock boundaries.

distributed between Y,Z= ±5 R$_M$ with the same density and bulk velocity used as inputs to LatHyS and AIKEF. The H$^+$ ion density distribution simulated with LIZE differ by less than 10% compared to Figure 3a and 3e. This is an indication that our method to reconstruct the ion density in LIZE yields accurate result.

3.3. Ion density

3.3.1. FIPS data analysis

FIPS was a TOF ion mass spectrometer with the ability to detect ions with m/q = 1-40 amu/e and an energy-per-charge E/q between 0.046 - 13.6 keV with 64 exponentially spaced energy channels (Andrews et al., 2007; Gershman et al., 2013). The effective field-of-view (FOV) of the instrument (1.15π sr) permit detection of ions coming from a wide range of directions with an angular resolution of 15°. During normal operation mode FIPS completed a scan of the full E/q range every 65 s. The second operation mode, the burst mode, was used to make frequent scans every 10 s (Gershman et al., 2013).

We extend the analysis by Raines et al. (2013) to the whole set of FIPS ion density (n$_{obs}$) observations accumulated between 23 March 2011 and 30 April 2015. Following Figure 3 in Raines et al. (2013), we plot the average ion density distribution of the Na$^+$- and O$^+$-group ions and He$^+$ as a function of local time and altitude (see the top row of Figure 3.3.1). We restrict our analysis to the latitude range ±30° centered on the equatorial plane. We use a grid with 0.5 h resolution in local time and 100 km in altitude identical to the grid that was used to make Figure 3 in Raines et al. (2013). The color map and color scale in Figure 3.3.1a-c is also identical to Figure 3 in Raines et al. (2013).

There exists two main enhancement regions in Figure 3.3.1a-b. The low-altitude enhancement extends between 6 - 12 local time and up to an altitude of 2000 km. The second, high-altitude enhancement extends between 16.5 - 21 h up to 6000 km. Both enhancement regions roughly follow the altitude profile of the magnetopause, but extends farther into the magnetosheath around noon. He$^+$ exhibits a low-altitude enhancement region at dawn similar to those observed for the Na$^+$ and O$^+$-group ions, but no high-altitude dusk enhancement. There also exists a narrow enhancement region located inside the magnetosheath at 18 h (altitude 5000-8000 km) for all three ion species. This enhancement feature is either missing or not as prominent in the (Raines et al., 2013) data set.

The observed ion density (n_{obs}) by FIPS is defined as

$$\sum_i f_i v_i^2 (\Delta v)_i \Delta \Omega \tag{1}$$

where f is the phase space density (PSD), v is the velocity, Δv is the velocity range, i corresponds to the index of the E/q step in FIPS operation and $\Delta \Omega$ is FIPS solid angle. The product between f_i and $v_i^2 (\Delta v)_i$ is summed over each
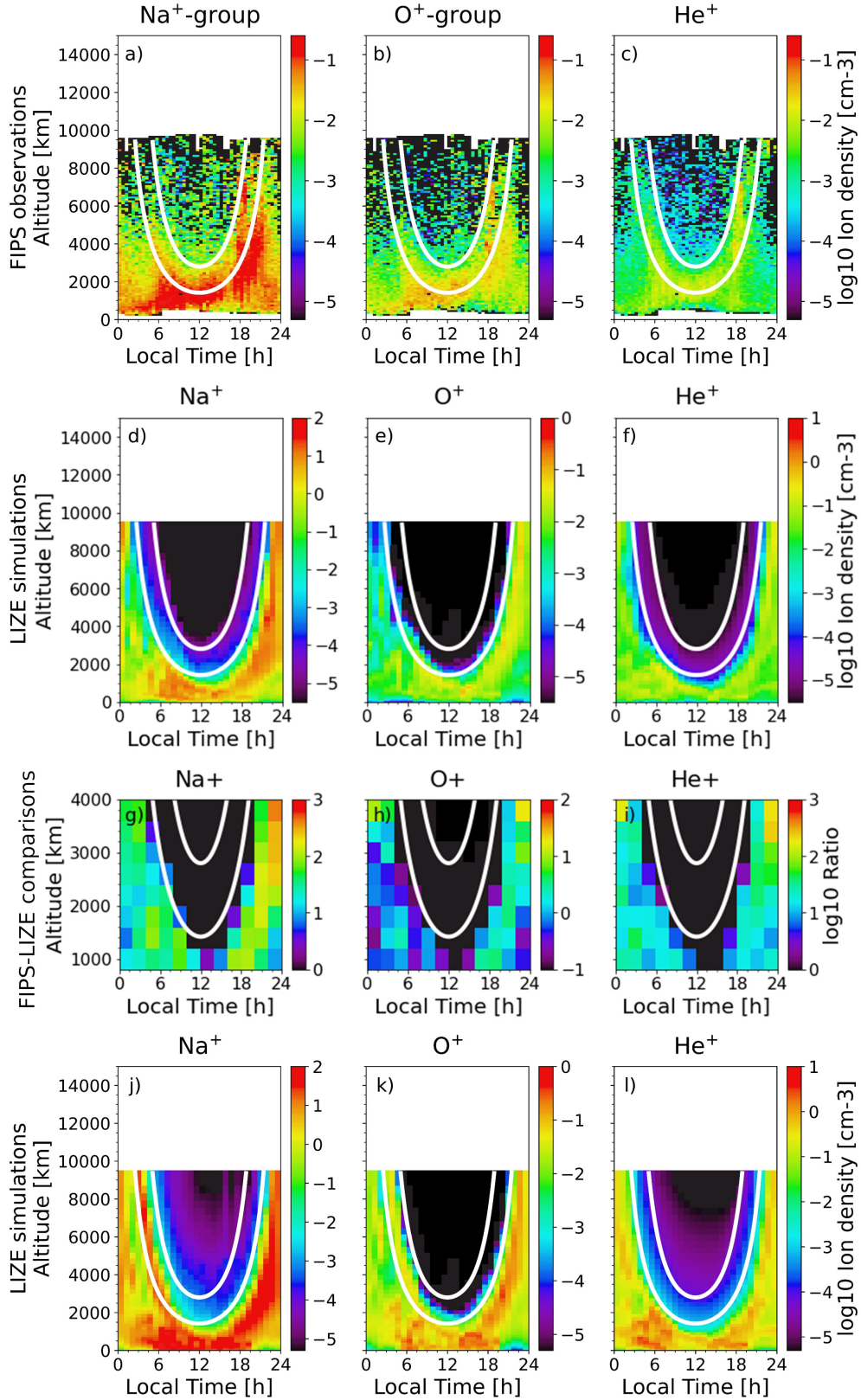
Figure 4: (Previous page.) Top row: The average observed ion density by FIPS of the (a) Na$^+$ group, (b) O$^+$ group and (c) He$^+$ in the latitude range $\pm 30°$. Second row: Simulated ion density of (d) Na$^+$, (e) O$^+$ and (f) He$^+$ with LIZE using the static magnetic and electric field description by LatHyS, including FIPS energy range and FOV constraints. Third row: Ratio between between the energy range and FOV-corrected simulated ion density and the observed ion density (grid resolution: 400 km, 2 h). The average ion density ratio below the magnetopause is 18 for Na, 0.25 for O and 5.2 for He. Bottom row: the full ion density (no energy range or FOV constraints) simulated with LIZE. The FIPS observations were accumulated between 23 March 2011 and 30 April 2015. The solid white lines show the magnetopause and bow shock boundaries as determined from Winslow et al. (2013). Do note that the sense of the magnetospheric boundaries are reversed in this Figure compared to Figure 3. Thus, points that appear to be located "inside" the parabolas in this Figure are in fact located outside the magnetosphere.

E/q step i in the FIPS energy range and FIPS effective FOV ($\Delta\Omega \approx 1.15\pi$ sr). n_{obs} is provided for both solar wind ion species (H$^+$ and He^{++}) and several planetary ion species (Na$^+$-, O$^+$-group ions and He$^+$).

Note that n_{obs} in Raines et al. (2013) was defined slightly differently from Equation 1, in that they did not include the FIPS FOV solid angle in the calculation. Therefore there is at least a 1.15π factor difference in magnitude between Figure 3 in Raines et al. (2013) and 3.3.1 in this paper. The lower energy limit of the FIPS burst observations was decreased from 100 eV to 46 eV in February 2012 (Raines et al., 2013). However, our analysis of the full mission FIPS data set showed very few counts below 100 eV, so the effect of this change is likely very minimal.

Recovered densities from FIPS are also available which make use of techniques to account for the limited FOV under certain assumptions (Raines et al., 2013; Gershman et al., 2013). We did not compare to these densities since they are not available in all regions.

3.3.2. Ion density simulations

The bottom row of Figure 3.3.1 shows the simulated He$^+$, O$^+$ and Na$^+$ ion density from LIZE using the LatHyS electric and magnetic field description. We use the full simulated energy range between $1 - 10^5$ eV. Due to the limited size of the $X > 0$ domain in the AIKEF simulation, we put an upper limit on the simulated ion densities to an altitude of 9500 km. Note that the ion density scale in the top and bottom row of Figure 3.3.1 are different, due to the high simulated densities.

The simulated ion density profiles do not match the absolute magnitude of the FIPS observations. However, both the dawn and the dusk enhancement regions are qualitatively well reproduced. The simulated ion density is highest near the surface (9.3×10^1 Na$^+$/cm^3, 2.1×10^{-1} O$^+$/cm^3 and 1.6 He$^+$cm^{-3}) where the dawn enhancement region is located (04 - 10 h local time). The corresponding FIPS values are: 2.7×10^{-1} Na$^+$/cm^3, 3.4×10^{-2} O$^+$/cm^3 and 1.3×10^{-2} He$^+$/cm^3. The simulated ion density in the magnetosheath is less dense and less extended with altitude compared to the observations. We next consider the effect of FIPS' limited FOV and energy range (0.046 - 13.6 keV) on the simulated ion densities.

The main limitation to FIPS nominal FOV (1.4 π sr) is caused by the sunshade of the spacecraft. The sunshade always points along the positive MSO X-axis irrespective of where the spacecraft is located relative to Mercury. This means that the true FOV extends between 15° from directly behind the sunshade up to 45° from the rear. The FOV is also partially blocked by one of the solar cell panels and other smaller parts on the spacecraft, so that the effective FOV solid angle is 1.15π sr. Since this study considers the ion density distribution averaged over several Mercury years we only consider the main limitations to the FOV along the MSO X-axis (see Figure 5).

The FIPS clock angle, which is defined as the angle between the positive MSO Y-axis and the FIPS boresight, describes the rotation of the spacecraft relative to the MSO frame. Specifically, this defines whether one hemisphere is sampled more than the other. The clock angle distribution for FIPS measurements taken within 0.15 R_{M} of the geometric equator between 2011-2015 is almost equal between the dusk and dawn hemispheres. Therefore, we can assume that FIPS samples both MSO Y-hemispheres in the latitude range $\pm 30°$. Due to MESSENGER's highly elliptic polar orbit, the lowest (highest) altitude range in Figure 3.3.1 (top row) will be mostly sampled when the spacecraft is moving toward the north (south) pole. Therefore, the lowest (highest) altitude range may be dominated by ions with $v_z < 0$ ($v_z > 0$). In this study we make the assumption that the FIPS instrument samples MSO $Z > 0$ and $Z < 0$ equally. The ions in our model tend to have small v_z velocities so the specified selection effect is likely not significant near the equatorial plane (see Section 4.4 where we will discuss the ion velocity distribution in greater detail).

The new simulated Na$^+$, O$^+$ and He$^+$ ion density maps that have been corrected for FIPS limited energy range and
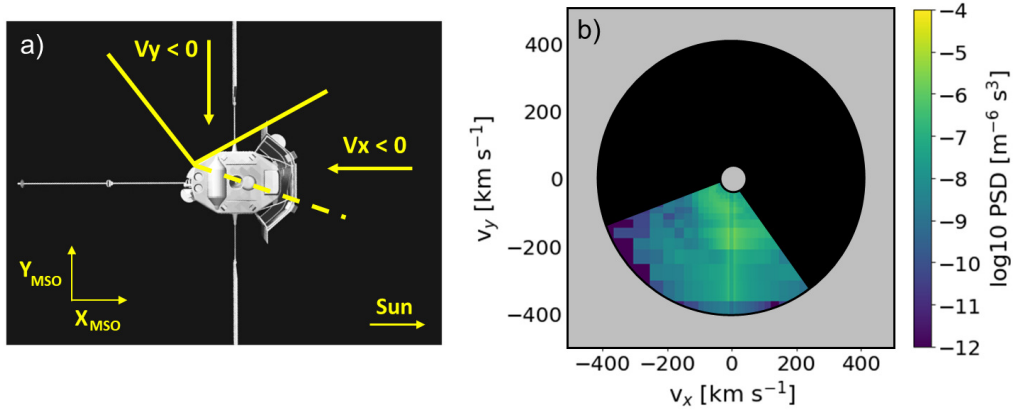
Figure 5: Approximation of (a) FIPS field-of-view (FOV) and the (b) effect of the FIPS energy range (grey) and FOV constraints (black) on an example phase space distribution in the MSO XY plane. The dashed line in (a) shows the extent of FIPS nominal FOV, which is partially obstructed by the sunshade. The model of MESSENGER in Figure 5a was adapted from "Interactive 3D model of the MESSENGER probe" by Fac-tory-o (https://commons.wikimedia.org/w/index.php?curid=71265802) under a Creative Commons (CC BY-SA 4.0) licence.

FOV are shown in the second row of Figure 3.3.1. The average ion density has decreased for all species but density enhancement between 18 - 24 h remains. The dawn hemisphere now exhibits a sharp drop-off in ion density before 6 h, similar to what is observed in the FIPS data (top row of Figure 3.3.1). We continue our comparison by making a ratio (see the third row of Figure 3.3.1) between the new simulated and observed ion density. We use a grid with coarser resolution (2 h, 400 km) and reduce the altitude range to 800-6000 km (to exclude bins with few FIPS observations). The average ion density ratio below the magnetopause is 18 for Na+, 5.2 for He+ and 0.25 for O+.

In this study, we have used two hybrid models. On average, AIKEF yields slightly higher ion densities compared to LatHyS but the spatial distribution is nearly identical (see Figure 6). One of the key differences between the two models is a low-altitude (< 1000 km) enhancement region which exists at all local times for AIKEF.

4. Discussion

4.1. Comparison with previous simulations of the Na+ density

When we compare our uncorrected ion density estimate (see Figure 3.3.1d-f) with previous modeling studies of the Na+ ion density distribution in Mercury's magnetosphere (Leblanc et al., 2003; Yagi et al., 2010; Seki et al., 2013; Exner et al., 2020) we find a similar order of discrepancy between the different models and the observations. Leblanc et al. (2003) used the exospheric model described in Leblanc and Johnson (2003) with the analytic magnetospheric model by Delcourt et al. (2003) to trace Na+ ions inside the magnetopause boundary. They found a maximum Na+ density of $10^2/cm^3$ at aphelion ($TAA = 180°$), which is close to our uncorrected simulated Na+ density (see Figure 3.3.1). Paral et al. (2010) found a maximum Na+ ion density on the order of $10\,cm^{-3}$ in the equatorial plane for an IMF with a strong northward component. Yagi et al. (2010) modeled the Na+ density for purely northward IMF ($B_z = 10$ nT) with the neutral exosphere model from Leblanc and Johnson (2003) and a MHD magnetospheric model to describe the electromagnetic field environment. Their Case 1 ($n_{sw} = 30\,cm^{-3}$, $v_{sw} = 400$ km/s) results gives a similar Na+ density in the dawn hemisphere ($10^2\,cm^{-3}$). Seki et al. (2013) studied the impact of varying southward IMF strength and planetary conductivity on the Na+ ion density distribution using an MHD magnetospheric model. Exner et al. (2020) studied the impact of successively denser versions of a Na+ exosphere on the Mercury field environment. For the standard exosphere they found a maximum Na+ density of $10/cm^3$ at the cusps. What is common for all these studies is that the modeled maximum Na+ density is a factor of $10 - 10^3$ times too high compared to the FIPS observations.

Sarantos et al. (2009) used the exospheric Na model from Mura et al. (2007), with a maximum Na surface density of $10^5\,cm^{-3}$ and a MHD simulation with the solar wind IMF profile of the first MESSENGER flyby Benna et al. (2010) to model the distribution of Na+ pickup ions. They studied the ion density distribution of Na+ produced from neutral Na ejected by different source mechanisms. Sarantos et al. (2009) derived a maximum Na+ density of $1\,cm^{-3}$, which is relatively similar to the observed Na+ ion density by FIPS compared to other modeling studies. The MHD simulation
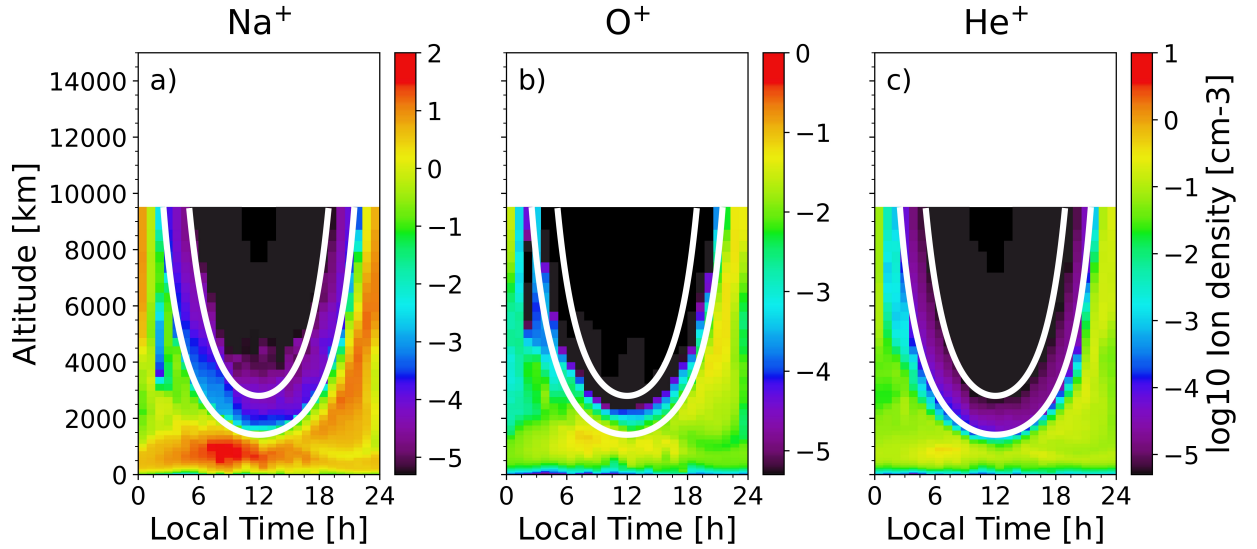
Figure 6: The (a) Na$^+$, (b) O$^+$ and (c) He$^+$ ion density simulated with LIZE using the static magnetic and electric field description by AIKEF.

used in Sarantos et al. (2009) simulation has a lower spatial resolution (122-1952 km) compared to the magnetospheric models in our study. Perhaps for this reason the mean energy of the Na$^+$ plasma sheet ions in their simulation is 10^2 times higher than in our simulation (see Figure 4 in Sarantos et al., 2009).

4.2. Comparison with other estimates of the ion density

It is also possible to derive the Na$^+$ density distribution around Mercury from the study of magnetic field-line-resonance (FLR) events (James et al., 2019). FLR events occur when a fast-mode MHD wave converts into a shear Alfvén wave in a non-uniform plasma environment. If this occurs near Mercury's dipole magnetic field, the resonant wave coupling may cause the formation of a standing wave in the closed magnetic field lines, oscillating at the fundamental plasma frequency (Glassmeier et al., 2004). At Mercury a subset of these waves has a frequency that lies below the local Na$^+$ ion gyro frequency, which indicates that the field line resonance is formed in a plasma dominated by Na$^+$ ions. James et al. (2019) identified such events using MAG data, the KT17 magnetic field line model (Korth et al., 2015, 2017) and a simple power-law model of the plasma mass density to map the ion density inside the closed field-line-region in the dayside magnetosphere. The plasma density estimate that can be inferred using this method is not limited by a specific energy range or FOV. Using a relaxed Earth-type FLR event criteria James et al. (2019) inferred a maximum plasma mass density of 500 amu/cm^3, which would imply a dayside Na$^+$ surface density of approximately 22/cm^3 (Exner et al., 2020).

Figure 7 shows the Na$^+$ ion density in the equatorial plane in units of amu/cm^3 (comparable to Figure 6e in James et al., 2019). The contribution from He$^+$ and O$^+$ to the total plasma mass density is negligible. Although our simulated Na$^+$ density is higher compared to Figure 6e in James et al. (2019), the difference is considerably lower than direct comparison with the FIPS observations. Most importantly, the maximum simulated plasma mass density near the surface (550 amu/cm^3 or 24 Na$^+$/cm^3) is a close match to James et al. (2019)'s estimate.

Another in-situ observation we could refer to get some clues about the ion density magnitude in the Hermean magnetosphere are the Mariner 10 Mercury flybys. During the Mariner 10 flyby on 1974 March 29, the electrostatic analyzer took electron density measurements in Mercury's plasma wake (Ogilvie et al., 1974). The spacecraft entered the magnetosphere from dusk in the southern magnetospheric lobe and exited at dawn in the north. The spacecraft reached a minimum altitude of 700 km from the surface near midnight local time in the equatorial plane at closest approach.

We model the Na$^+$, O$^+$, He$^+$ and solar wind H$^+$ ion density with LIZE along the trajectory of Mariner 10. For the electric and magnetic fields, we use the northward B_z LatHyS simulation with $n_{sw} = 45.7$/cm^3 and $v_{sw} = 500$ km/s from the end of Section 3. The solar wind properties of this run matches the observed electron energy spectra just
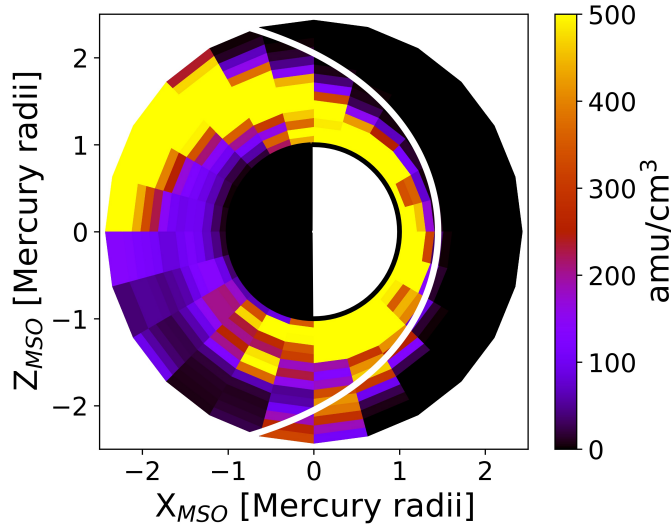
Figure 7: The simulated Na$^+$ ion density in the equatorial plane expressed in amu/cm^3 and plotted with the same color map and in the same scale as Figure 4e and 6e in James et al. (2019).

467 prior to the spacecraft's entry into the magnetosphere (Ogilvie et al., 1974). We compare the observed electron density
468 with the different simulated ion densities (full energy range and FOV) between 20:41-20:47 UTC which is when the
469 spacecraft first enters the planet's shadow until the time of closest approach. We find that the modeled Na$^+$ ion density
470 in this region is much smaller (0.5-1.0 Na$^+$/cm^3) than the H$^+$ (3.7-9.0 H$^+$/cm^3) or the electron density (< 6.2 e/cm^3).
471 The He$^+$ and O$^+$ densities are negligible. The comparatively low Na$^+$ density implies that the model does not give
472 results which directly contradicts the Mariner 10 electron density observations.

473 **4.3. Intrinsic limits of our simulated ion density**

474 In our EGM simulation of the Na exosphere the near-surface density is $\sim$ 5 times higher at the dawn terminator
475 compared to the subsolar point. The EGM model reproduces the dusk-dawn asymmetry at aphelion observed by UVVS
476 Cassidy et al. (2016). UVVS and THEMIS observations of the Na exosphere near aphelion indicates however that the
477 maximum Na density in the exosphere is located near the subsolar point Milillo et al. (2021); Cassidy et al. (2016).
478 This discrepancy is unlikely to affect the large-scale ion density distribution due to the fast configuration speed of the
479 ions.

480 Due to the special geometry of the MESSENGER orbit, the ion density at each local time was sampled by FIPS
481 at a particular TAA. The data at 6 - 12 h local time was, for instance, taken when Mercury was located between
482 TAA= 0° − 90°. The Na exosphere has a strong dawn peak during this part of the orbit (Cassidy et al., 2015, 2016),
483 which might help explain the Na$^+$ enhancement at dawn in Figure 3.3.1a.

484 The static electromagnetic field environments used in our study may be responsible for the large underestimation
485 of the ion density upstream of the magnetopause (Figure 3.3.1). Without a time-dependent electromagnetic field
486 description it is not possible to account for temporal variations of the position of the magnetic boundaries, magnetic
487 reconnection and other plasma processes.

488 The average O$^+$ ion density in our simulation is low in comparison to Na$^+$ or He$^+$. Since the O$^+$-group includes
489 several species it is possible that O$^+$ is not the main constituent of the total O$^+$-group ion density (Vervack et al.,
490 2016). It may therefore be necessary to consider the photo-ionization of water ices on Mercury. The Na$^+$-group
491 includes several ion species with similar mass-per-charge ratio to Na$^+$, which includes Mg$^+$, Al$^+$ and Si$^+$. The neutral
492 Mg exosphere is thin (5-50/cm^3 at the surface; Merkel et al., 2017) and the Mg photo-ionization rate (6.5×10^{-7} s^{-1};
493 Huebner and Mukherjee, 2015) is low compared to Na. Therefore Mg$^+$ is unlikely to make a large contribution to the
494 total Na$^+$-group ion density. Evans et al. (2012) inferred a Si (weight) surface abundance of 24.6% with observations
495 by the Gamma-Ray and Neutron Spectrometer (GRNS) on MESSENGER, which corresponds to a number density
496 that is approximately half that of Na. Al has been observed in Mercury's exosphere with ground-based observations
497 (Bida et al., 2000; Bida and Killen, 2017) and by MESSENGER (Vervack et al., 2016). In adddition, both Al and Si

Table 4

Parameters of the LIZE simulations with different solar wind and IMF conditions. The ion density ratio is defined as the average ratio between the simulated and observed ion density in the altitude range 800-6000 km and below the magnetopause boundary.

Parameter	Nominal case	Case 1	Case 2	Case 3
Time step:	0.02 s	0.05 s	0.05 s	0.05 s
Spatial resolution:	145 km	112 km	112 km	237 km
Number of solar wind particles per cell:	H^+: 20 He^{++}: 2	H^+: 5 He^{++}: 2	H^+: 5 He^{++}: 2	H^+: 5 He^{++}: 2
Solar wind number	30 cm^{-3}	50 cm^{-3}	50 cm^{-3}	11 cm^{-3}
Solar wind velocity:	400 km/s	500 km/s	400 km/s	400 km/s
Solar wind magnetic field (B_x, B_y, B_z) [nT]:	(0, 0, 20)	(- 10, 7.5, 13)	(-9.3, 7.7, -13)	(-9.3, 7.7, -13)
Ion density ratio:	Na^+: 18 He^+: 5.2	Na^+: 2.7 He^+: 1.1	Na^+: 1.6 He^+: 0.8	Na^+: 0.8 He^+: 0.5

498 have very high photo-ionization rates (Al: 1.2×10^{-3} s^{-1} and Si: 2.29×10^{-5} s^{-1}; Huebner and Mukherjee, 2015)
499 compared to Na. Jasinski et al. (2020)'s estimate of the Al and Si ion production rate (3-7.5/cm^3 at 1500 km) during
500 a large meteoroid impact event can be considered as an upper limit.
501   Our simulated ion densities reflect a single set of solar wind plasma conditions, IMF orientation and orbital phase.
502 In comparison, the FIPS data displayed in Figure 3.3.1a-c represent an average over 17 Mercury years of observations,
503 and accounts for a wide range of solar wind and exospheric conditions. As the FIPS data reflect the average state of
504 the exosphere, some features may not be as prominent in the FIPS observations as in the simulated ion density. The
505 dusk enhancement region is very dense compared to other regions in our simulation and extends to higher altitudes
506 compared to the observations. This may be an effect of the electric field environment that the test-particle encounter at
507 the flanks of the dayside magnetopause boundary. For solar wind IMF $B_z > 0$ we get $E_y < 0$ in the solar wind (and the
508 magnetosheath). Ions that encounter the duskside magnetopause flank are affected by a strong $E_x < 0$ environment
509 and $E_y < 0$, which will cause these ions to be pushed deep into the low electric field environment of the nightside
510 plasma sheet. The pink-purple Na$^+$ test-particle trajectory in Figure 8 shows an example of this effect. Ions that
511 approach the magnetopause flank from the dawnside experience $E_x > 0$, which makes them more likely to be picked
512 up by the solar wind and quickly escape the Mercury environment. Therefore, for the specific solar wind IMF studied
513 here we will naturally get a low-density, high-energy dawnside ion population and a high-density duskside. The dusk
514 enhancement could also be be due to the non-adiabatic ion acceleration mechanism described in Delcourt et al. (2003),
515 but the northward IMF B_z may inhibit its effects. The blue-cyan Na$^+$ test-particle trajectory in Figure 8 shows a
516 possible example of this acceleration mechanism in action. The sudden increase in energy after 4 minutes when the
517 test-particle was located close the surface near the north pole indicates that it may have experienced centrifugal ion
518 acceleration (compare to Figure 2 in Delcourt et al., 2003).
519   The strictly northward solar wind IMF and the low solar wind ram pressure of the electromagnetic field envi-
520 ronment considered in this work is not necessarily the most commonly observed solar wind environment at Mercury
521 (Sarantos et al., 2007). In order to consider the impact of different solar wind conditions on the modeled ion density,
522 we model Na$^+$, O$^+$ and He$^+$ using three additional LatHyS simulations (see Table 4). We find that the average ion
523 densities computed from these simulations are much closer to the observed values. The difference between model and
524 observations range between a factor of 0.8-1.5 for Na$^+$ and 0.5-1.1 for He$^+$. The O$^+$ density tends to be underesti-
525 mated. However, although the average ion density ratio is improved the spatial distribution is very different from our
526 nominal case. Following the argument concerning the sign of $E_x, /E_y$ and their impact on the properties of the ion
527 populations on either side of the nightside plasma sheet, we find that Cases 1-3 result in weaker dusk- and stronger
528 dawn enhancement than expected from the FIPS observations. The LatHyS simulations corresponding to Cases 1-3
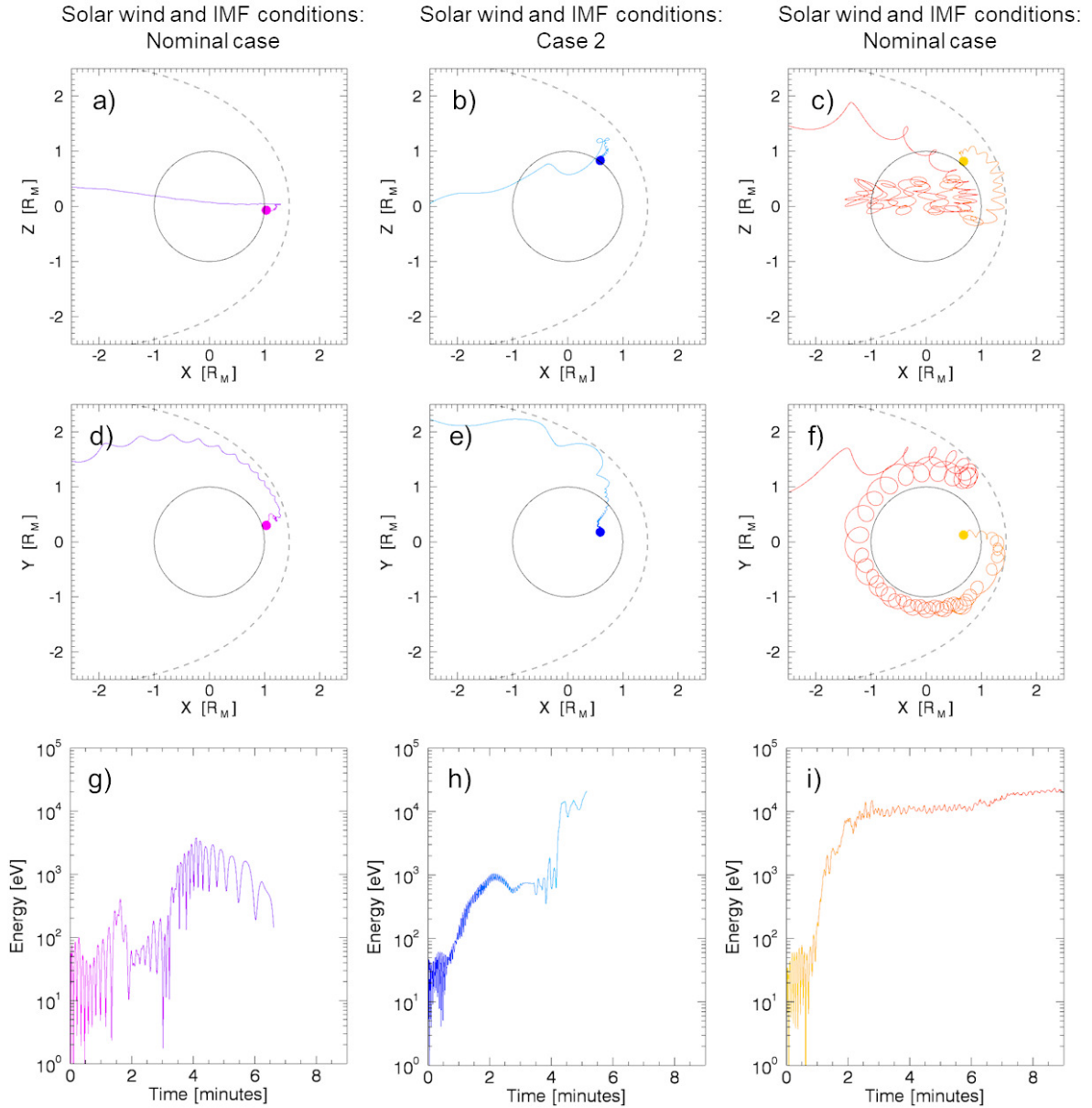
Figure 8: Model test-particle trajectories of Na^+ ions from the Latmos IoniZed Exosphere model in the (a-c) MSO XZ-plane and the (d-f) XY-plane. The time-evolution of the test-particle ion energy are shown in (g-i). The dashed curves in (a-f) shows the average location of Mercury's magnetopause. The three test-particles were launched in the dayside magnetosphere (b, c) near the north pole and (a) near the subsolar point (start location shown by the dot markers). The test-particles experience different electromagnetic fields: (a, c) solar wind and IMF conditions corresponding to the nominal case in Table 4 and (b) Case 2 in Table 4. The color gradient in each trajectory shows the evolution of time.

have a lower resolution compared to our nominal case, which may result in higher electric fields in low-density regions inside the magnetosphere which would result in higher test-particle acceleration and lower densities. Regardless, it is clear that the ion density distribution of heavy ions around Mercury have the potential of being highly variable. Since the ion density observations by FIPS discussed in this paper reflects a wide range of solar wind and exosphere conditions, it may be necessary to test more representative solar wind and IMF conditions in order to re-produce the observed distribution as closely as possible.

Global models of Mercury's magnetosphere tend to underestimate the magnetopause reconnection rate for north-ward solar wind IMF boundary conditions. In effect, this likely causes the average level of Dungey cycle circulation (Dungey, 1961) to be underestimated. Therefore the planetary ion population in our nominal $B_z > 0$ simulation may experience an uncharacteristically weak electric field environment. This aspect could partly explain why we're seeing such a large factor difference between our model results and the FIPS observations for that specific IMF orientation. The low-altitude enhancement in the modeled ion density profiles with AIKEF may be an another effect of the under-estimated ion dynamics on the magnetosphere. This ion population is comparatively energetic (10^4 eV) compared to ions at higher altitudes and may be the result of a quasi-trapped ion ring, similar to what has been proposed in Yagi et al. (2010, 2017). Indeed, the the yellow-orange Na$^+$ test-particle trajectory in Figure 8 and other test-particle trajec-tories in this region show a remarkable similarity to Figure 10 in Yagi et al. (2010) and Figure 3 in Yagi et al. (2017) respectively. The large magnetopause standoff distance during northward IMF and the steady-state magnetospheric fields used in our simulations are likely favorable for the formation of a quasi-steady ring distribution. If the IMF is southward or the short-term variability of the IMF is accounted for the ring distribution may not be as complete as indicated here.

4.4. Reconstruction of the phase space density (PSD)

Judging from Figure 3.3.1j-l the ratio between the simulated and the observed ion densities are not homogeneous. The simulated ion densities tend to diverge more from the observed values with increasing distance from the surface, which is most evident at midnight local time. The ratio is higher in the dusk enhancement region than at dawn, and it is very low near the magnetopause boundary at noon. To investigate the impact of FIPS FOV on the ion density distribution in the magnetosphere in more detail it is necessary to model the phase space density (PSD) distribution.

We model the PSD distribution in four different regions and investigate how FIPS energy range and FOV affects the sampling of the simulated ion density distribution. We select regions located at noon and the dawn enhancement region in the dayside magnetosphere, the dusk enhancement region on the nightside and the dawn magnetosheath (see Figure 9a). The four regions are all centered in the magnetic equatorial plane and range in size between $(\Delta x)^3 = (300 \text{km})^3$ to $(\Delta x)^3 = (750 \text{km})^3$. Inside the magnetic equatorial plane the FIPS clock angle is such that the boresight of the instrument is predominantly directed toward the dusk hemisphere (approximately 4 times more frequently). Therefore we will only consider the $v_y < 0$ sector in the $v_x - v_y$ plane (see Figure 9). We first compute the PSD on a spherical grid (E, θ, ϕ) with LIZE and then make a transformation to Cartesian velocity coordinates (v_x, v_y, v_z). This allows us to plot $v_x - v_y$ and $v_x - v_z$ slices of the 3-D PSD distribution.

As shown by Figure 9, the Na$^+$ PSD has a distinct spatial distribution in each of the four region. The PSD in Region A is dominated by a dawnward ($v_y < 0$) drift (see Figure 9b). The proximity of Region A to the magnetopause and the strong influence of the dawn- and anti-sunward drift of the solar wind convection field near Region A may be the cause of this particular distribution. Since the FIPS boresight is typically pointing toward the dusk hemisphere in this region, it is well suited to sample a PSD of this type. However, a slice of the same PSD distribution in the $v_x - v_z$ plane reveals that the PSD is concentrated to a narrow region around the MSO X-axis that is blocked from FIPS FOV by the sunshade (Figure 9c). This means that only a fraction of the PSD will be detected by FIPS despite the favorable distribution of the PSD in the $v_x - v_y$ plane. The distribution is far from being isotropic, yet the PSD tends to be more isotropic at lower energies (see Figure 9c).

Region B has a ring-like PSD distribution in the XY plane (Figure 9d) and is rather isotropic in the XZ plane (Figure 9g). Although the maximum of the PSD distribution in Region C (Figure 9e) appears to be located inside FIPS energy range, the global maximum is actually located below FIPS lower energy range (at approximately 10 eV). The PSD in Region D (Figure 9f) resembles a pick-up ion distribution. This implies that the Na$^+$ ions in Region D have been accelerated from outside the magnetopause into the dawn magnetosheath. The PSD distribution of this region peaks at velocities well outside the upper energy range of FIPS in both the $v_x - v_y$ and the $v_x - v_z$ plane, which makes the ions in this region invisible to FIPS.

Although the relative intensity of the PSD differs between the three different species, the spatial distribution is very similar in the MSO XY and XZ plane (see Figure A1-A3 in the appendix). The PSD distribution in Region D has been omitted for O$^+$ due to poor statistics. It is interesting to note that in contrast to Na$^+$, the He$^+$ PSD distribution in Region D falls inside the upper limit of FIPS energy range. In the XZ plane, the PSD distribution is generally concentrated to the non-observable part of phase space for FIPS. The PSD in Region B has the most dispersion in the XZ plane, likely because this region is located far away from the planet and the ions transported here have had more time to disperse. On average LatHyS and AIKEF yields very similar PSD distributions. One key difference between the two models is that
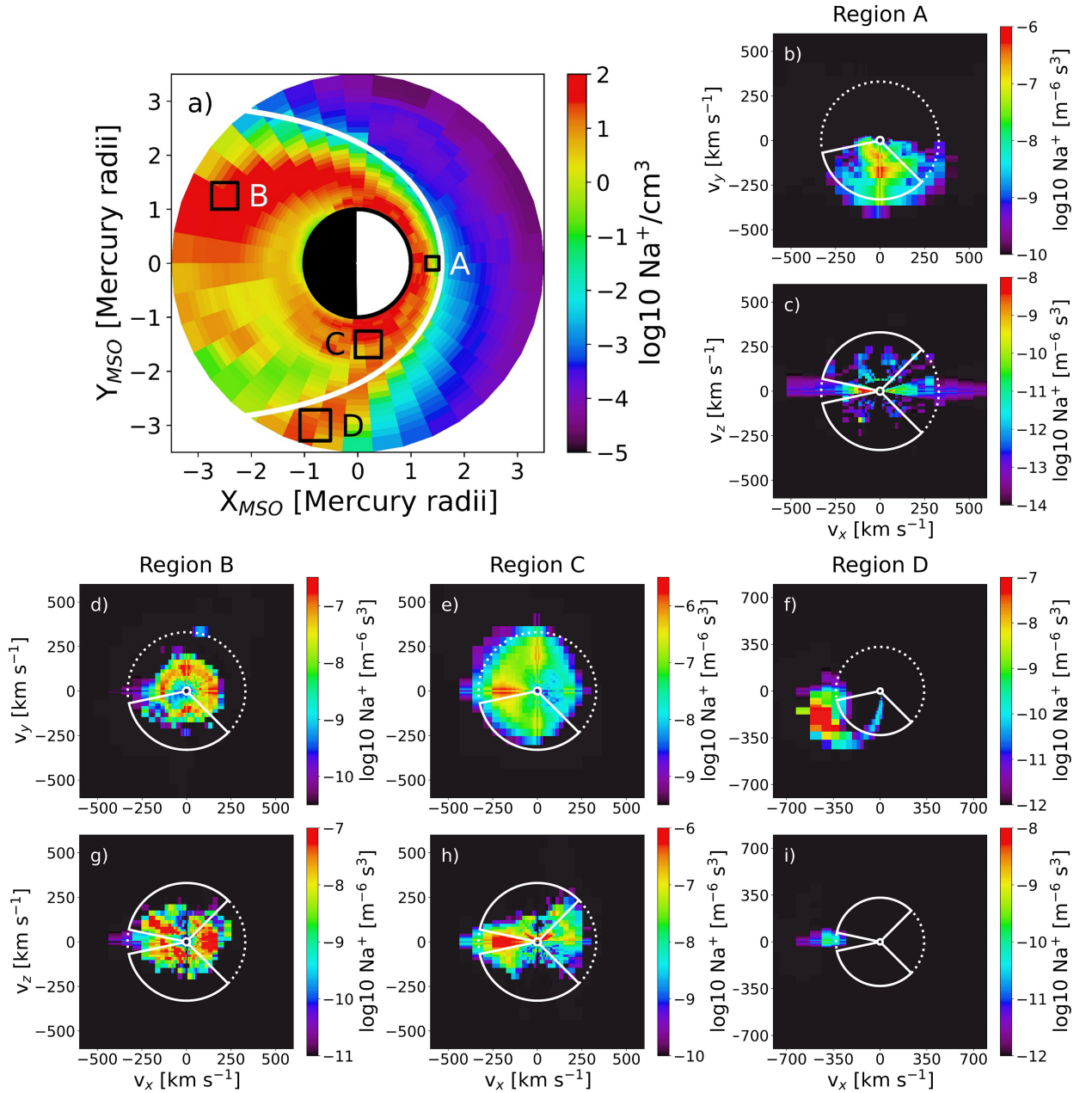
Figure 9: (a) Location of Regions A-D and the uncorrected Na⁺ ion density in the equatorial plane. Selected cuts of the Na⁺ PSD in the (b-c) MSO $v_x - v_y$ plane ($v_z = 0$) and the (d-g) $v_x - v_z$ plane ($v_y = 0$). The dotted circles in (b-g) mark the lower and upper energy limit of the FIPS energy range. The circle sectors marked with solid lines illustrate the FIPS limited FOV.

the PSD computed with AIKEF in Region B is concentrated to lower energies in the XY plane and is less dispersed in the XZ plane compared to LatHyS. This suggests that the electric field in Region B is lower in the AIKEF simulation than for LatHyS. Indeed, the anti-sunward component of the electric field in the AIKEF simulation is -0.09 mV/m in Region B compared to -0.8 mV/m for LatHyS.

5. Conclusions

We have analyzed the average ion density and spatial distribution in the equatorial plane inside Mercury's magnetosphere of the Na$^+$-group, O$^+$-group and He$^+$, which were observed by FIPS onboard MESSENGER during the whole orbital mission from 23 March 2011 to 30 April 2015. We developed a test-particle model that describes the full equation of motion of planetary ions produced from photo-ionization of Mercury's neutral exosphere. The model is coupled to a test-particle model of the neutral exosphere (EGM; Leblanc et al., 2017b) and two hybrid models of the electric and magnetic fields in the magnetosphere (LatHyS and AIKEF; Modolo et al., 2016; Müller et al., 2012). We modeled the neutral Na, O and He exospheres at aphelion with EGM and used static electromagnetic field simulations from the two models using the same set of solar wind input parameters to model the ionized Na$^+$, O$^+$ and He$^+$ exospheres for northward IMF conditions. We take the FIPS energy range and FOV constraints into account when we later compare our simulated ion densities with the FIPS ion density observations.

The model reproduces the spatial distribution of the FIPS observations but the average ion density (corrected for FIPS FOV) is between 5-18 times too high compared to the observations. These values were calculated for strictly northward IMF conditions ($B_z = +20$ nT), which might have caused the average Dungey cycle strength to be underestimated (and the ion density to be overestimated). The discrepancy between model and observations is lower (0.8-2.7 for Na$^+$ and 0.5-1.1 for He$^+$) for other solar wind and IMF conditions. The model based on a simple neutral O exosphere tends to underestimate the observed O$^+$ density. The magnitude of the simulated Na$^+$ density uncorrected for the FIPS energy range and field-of-view is roughly in agreement with previous simulation studies (Leblanc et al., 2003; Paral et al., 2010; Yagi et al., 2010; Seki et al., 2013; Exner et al., 2020) even for the nominal case ($B_z = +20$ nT). We also compare our results with plasma mass density measurements inferred from FLR event observations with the MAG instrument (James et al., 2019) and electron density measurements taken by Mariner 10 in the wake of the planet on 29 March 1974 (Ogilvie et al., 1974).

Finally, we model the phase space density distribution in four different regions: at noon and dawn in the dayside magnetosphere, in the dusk magnetotail and the dawn flank of the magnetosheath. We find that the PSD is commonly concentrated to a narrow region surrounding the v_x axis in the $v_x - v_z$ plane. This particular region in phase space is blocked from FIPS FOV due to MESSENGER's sunshade, meaning that only a fraction of the total PSD can be observed. Only the relative magnitude of the PSD distribution appears to be mass-dependent and the distribution in phase space is very similar between the three different species.

The results of this study highlight the limitations of using a steady-state electromagnetic field simulation to model the ion density distribution around Mercury. The phase space density distribution of heavy planetary ions are not necessarily isotropic and vary across different regions around Mercury. One of the largest assets of EGM is its capability to give an accurate description of the exosphere at several points along Mercury's orbit. The results by Raines et al. (2013); Jasinski et al. (2021) on the variation of the global Na$^+$-group ion density along the Mercury year may suggest there is a link between the seasonal neutral Na exosphere and the Na$^+$-group ion distribution in the magnetosphere. We plan to investigate this link with LIZE in more detail in future work.

BepiColombo, which will enter into orbit around Mercury in late 2025, will provide the first in-situ measurements around Mercury since the end of the MESSENGER mission in 2015. Planetary Ion Camera (PICAM) on the Mercury Planetary Orbiter (MPO) has an energy resolution between 1 eV - 3 keV and instantaneous 2π sr FOV (Orsini et al., 2010) and is uniquely suited to study low-energy ions near the surface and ions which have been recently formed. The Mercury Ion Analyzer (MIA) and the Mercury mass Spectrum Analyzer (MSA) on the Mercury Magnetospheric Orbiter (MMO; renamed to MIO after the launch) will be able to sample ions with a wide range of energies (5 eV/e - 30/40 keV/e; Saito et al., 2010). Both instruments have an instantaneous 8-10° × 360° of view, which will also make it possible to obtain the full three-dimensional distribution function of the observed ions. Finally, the UV spectrometer Probing of Hermean Exosphere By Ultraviolet Spectroscopy (PHEBUS; Chassefière et al., 2010) on MPO will make the first in-situ measurements of the neutral He exosphere since Mariner 10 and, for the first time, enable the study of the coupling between the neutral and ionized He exosphere.

6. Acknowledgments

A. Appendix

This appendix includes additional figures of the PSD distribution for Na$^+$ (Figure A1), O$^+$ (Figure A2) and He$^+$ (Figure A3). The figures show the PSD distribution in the MSO $v_x - v_y$ and $v_x - v_z$ plane for both the LatHyS and AIKEF. Figure A2 only includes Region A-C.
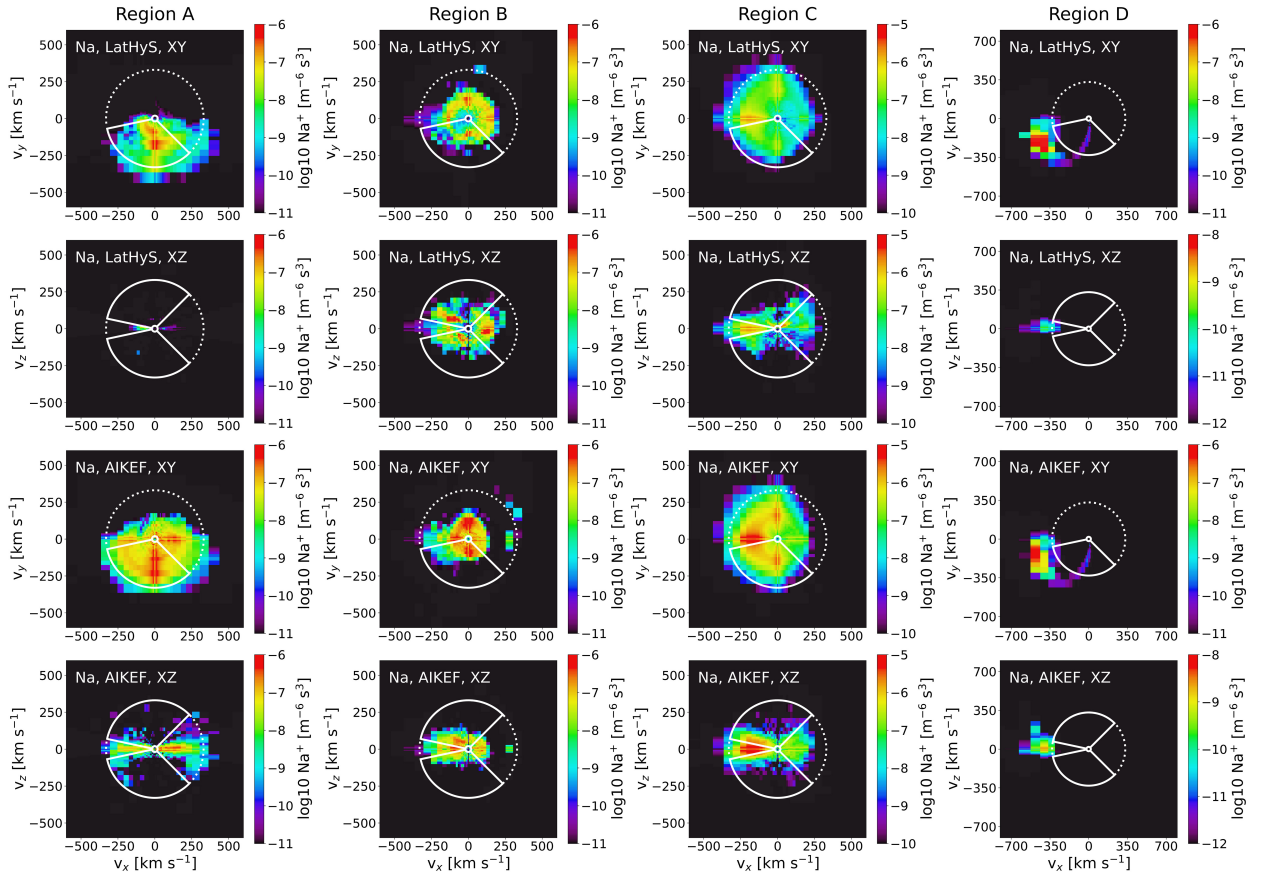

Figure 10: Slices of the Na$^+$ PSD in the MSO $v_x - v_y$ plane ($v_z = 0$) and the $v_x - v_z$ plane ($v_y = 0$) in Regions A-D computed with the magnetic and electric fields supplied by LatHyS and AIKEF.
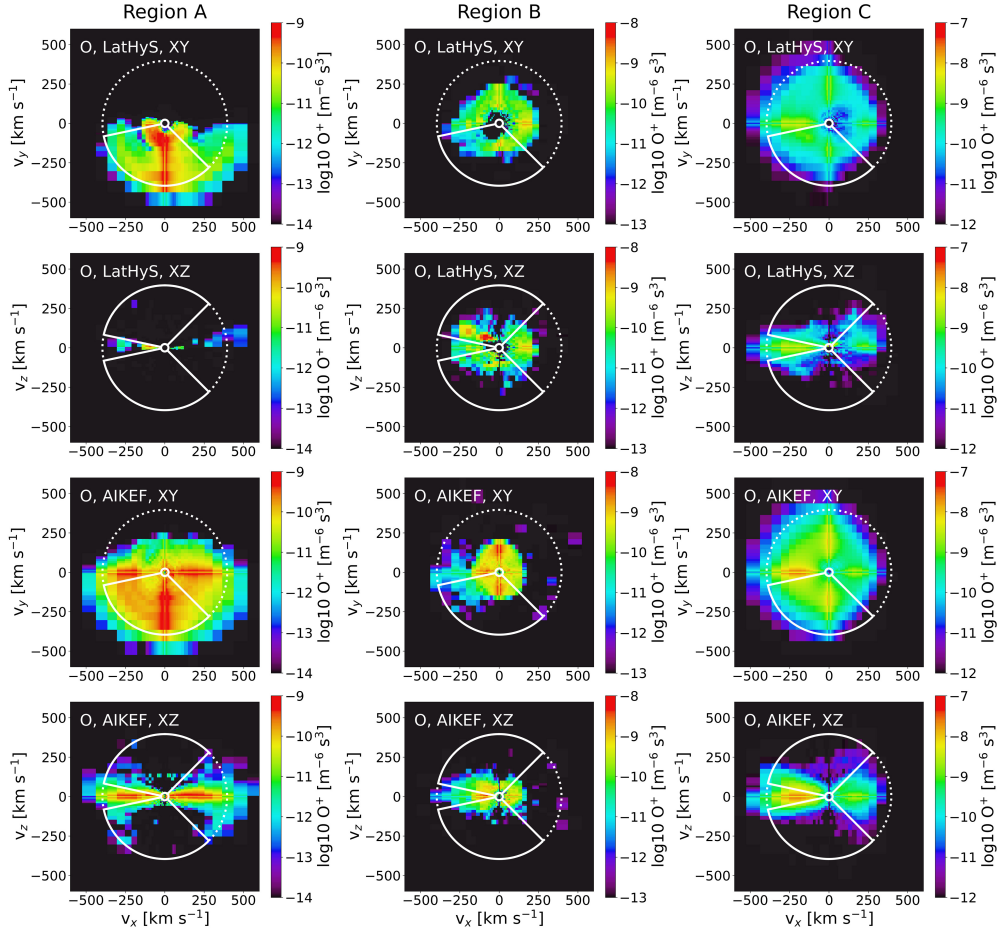
Ion density distribution of Na$^+$, O$^+$ and He$^+$ in Mercury's magnetosphere

Figure 11: Slices of the O$^+$ PSD in the MSO $v_x - v_y$ plane ($v_z = 0$) and the $v_x - v_z$ plane ($v_y = 0$) in Regions A-C computed with the magnetic and electric fields supplied by LatHyS and AIKEF.
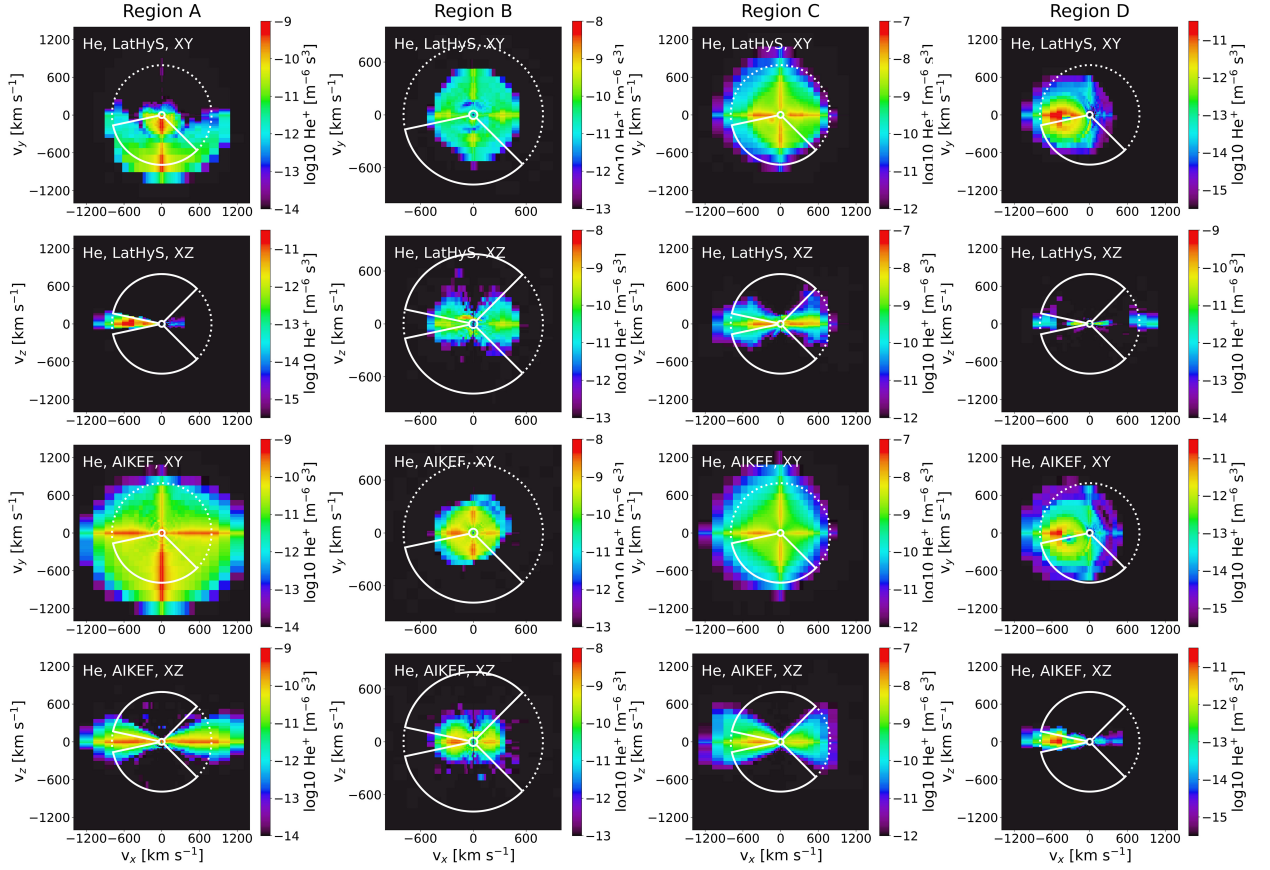
Figure 12: Slices of the He$^+$ PSD in the MSO $v_x - v_y$ plane ($v_z = 0$) and the $v_x - v_z$ plane ($v_y = 0$) in Regions A-D computed with the magnetic and electric fields supplied by LatHyS and AIKEF.

References

Aizawa, S., Griton, L.S., Fatemi, S., Exner, W., Deca, J., Pantellini, F., Yagi, M., Heyner, D., Génot, V., André, N., Amaya, J., Murakami, G., Beigbeder, L., Gangloff, M., Bouchemit, M., Budnik, E., Usui, H., 2021. Cross-comparison of global simulation models applied to Mercury's dayside magnetosphere. Planetary and Space Science 198, 105176. doi:10.1016/j.pss.2021.105176.

Anderson, B.J., Johnson, C.L., Korth, H., Purucker, M.E., Winslow, R.M., Slavin, J.A., et al., 2011. The Global Magnetic Field of Mercury from MESSENGER Orbital Observations. Science 333, 1859. doi:10.1126/science.1211001.

Andrews, G.B., Zurbuchen, T.H., Mauk, B.H., Malcom, H., Fisk, L.A., Gloeckler, G., Ho, G.C., Kelley, J.S., Koehn, P.L., Lefevere, T.W., Livi, S.S., Lundgren, R.A., Raines, J.M., 2007. The Energetic Particle and Plasma Spectrometer Instrument on the MESSENGER Spacecraft. Space Science Reviews 131, 523–556. doi:10.1007/s11214-007-9272-5.

Benna, M., Anderson, B.J., Baker, D.N., Boardsen, S.A., Gloeckler, G., Gold, R.E., et al., 2010. Modeling of the magnetosphere of Mercury at the time of the first MESSENGER flyby. Icarus 209, 3–10. doi:10.1016/j.icarus.2009.11.036.

Bida, T.A., Killen, R.M., 2017. Observations of the minor species Al and Fe in Mercury's exosphere. Icarus 289, 227–238. doi:10.1016/j.icarus.2016.10.019.

Bida, T.A., Killen, R.M., Morgan, T.H., 2000. Discovery of calcium in Mercury's atmosphere. Nature 404, 159–161. doi:10.1038/35004521.

Broadfoot, A.L., et al., 1976. Mariner 10: Mercury atmosphere. Geophysical Research Letters 3, 577–580. doi:10.1029/GL003i010p00577.

Cassidy, T.A., McClintock, W.E., Killen, R.M., Sarantos, M., Merkel, A.W., Vervack, R.J., Burger, M.H., 2016. A cold-pole enhancement in Mercury's sodium exosphere. Geophysical Research Letters 43, 11,121–11,128. doi:10.1002/2016GL071071.

Cassidy, T.A., Merkel, A.W., Burger, M.H., Sarantos, M., Killen, R.M., McClintock, W.E., Vervack, R.J., 2015. Mercury's seasonal sodium exosphere: MESSENGER orbital observations. Icarus 248, 547–559. doi:10.1016/j.icarus.2014.10.037.

Cassidy, T.A., Schmidt, C.A., Merkel, A.W., Jasinski, J.M., Burger, M.H., 2021. Detection of Large Exospheric Enhancements at Mercury due to Meteoroid Impacts. The Planetary Science Journal 2. doi:10.3847/PSJ/ac1a19.

Chassefière, E., Maria, J.L., Goutail, J.P., Quémerais, E., Leblanc, F., Okano, S., Yoshikawa, I., Korablev, O., Gnedykh, V., Naletto, G., Nicolosi, P., Pelizzo, M.G., Correia, J.J., Gallet, S., Hourtoule, C., Mine, P.O., Montaron, C., Rouanet, N., Rigal, J.B., Muramaki, G., Yoshioka, K., Kozlov, O., Kottsov, V., Moisseev, P., Semena, N., Bertaux, J.L., Capria, M.T., Clarke, J., Cremonese, G., Delcourt, D., Doressoundiram, A., Erard, S., Gladstone, R., Grande, M., Hunten, D., Ip, W., Izmodenov, V., Jambon, A., Johnson, R., Kallio, E., Killen, R., Lallement, R., Luhmann, J., Mendillo, M., Milillo, A., Palme, H., Potter, A., Sasaki, S., Slater, D., Sprague, A., Stern, A., Yan, N., 2010. PHEBUS: A double ultraviolet spectrometer to observe Mercury's exosphere. Planetary and Space Science 58, 201–223. doi:10.1016/j.pss.2008.05.018.

Delcourt, D.C., Grimald, S., Leblanc, F., Berthelier, J.J., Millilo, A., Mura, A., et al., 2003. A quantitative model of the planetary Na+ contribution to MercuryÂ's magnetosphere. Annales Geophysicae 21, 1723–1736. doi:10.5194/angeo-21-1723-2003.

Delcourt, D.C., Moore, T.E., Orsini, S., Millilo, A., Sauvaud, J.A., 2002. Centrifugal acceleration of ions near Mercury. Geophysical Research Letters 29. doi:10.1029/2001GL013829.

Dong, C., Wang, L., Hakim, A., Bhattacharjee, A., Slavin, J.A., DiBraccio, G.A., Germaschewski, K., 2019. Global Ten-Moment Multifluid Simulations of the Solar Wind Interaction with Mercury: From the Planetary Conducting Core to the Dynamic Magnetosphere. Geophysical Research Letters 46, 11,584–11,596. doi:10.1029/2019GL083180.

Doressoundiram, A., Leblanc, F., Foellmi, C., Erard, S., 2009. Metallic Species in Mercury's Exosphere: EMMI/New Technology Telescope Observations. The Astrophysical Journal 137, 3859–3863. doi:10.1088/0004-6256/137/4/3859.

Dungey, J.W., 1961. Interplanetary Magnetic Field and the Auroral Zones. Physical Review Letters 6, 47–48. doi:10.1103/PhysRevLett.6.47.

Evans, L.G., Peplowski, P.N., Rhodes, E.A., Lawrence, D.J., McCoy, T.J., Nittler, L.R., Solomon, S.C., Sprague, A.L., Stockstill-Cahill, K.R., Starr, R.D., Weider, S.Z., Boynton, W.V., Hamara, D.K., Goldsten, J.O., 2012. Major-element abundances on the surface of Mercury: Results from the MESSENGER Gamma-Ray Spectrometer. Journal of Geophysical Research (Planets) 117. doi:10.1029/2012JE004178.

Exner, W., Heyner, D., Liuzzo, L., Motschmann, U., Shiota, D., Kusano, K., Shibayama, T., 2018. Coronal mass ejection hits mercury: A.I.K.E.F. hybrid-code results compared to MESSENGER data. Planetary and Space Science 153, 89–99. doi:10.1016/j.pss.2017.12.016.

Exner, W., Simon, S., Heyner, D., Motschmann, U., 2020. Influence of Mercury's Exosphere on the Structure of the Magnetosphere. Journal of Geophysical Research: Space Physics 125. doi:10.1029/2019JA027691.

Fulle, M., Leblanc, F., Harrison, R.A., Davis, C.J., Eyles, C.J., Halain, J.P., Howard, R.A., Bockelée-Morvan, D., Cremonese, G., Scarmato, T., 2007. Discovery of the Atomic Iron Tail of Comet MCNaught Using the Heliospheric Imager on STEREO. The Astrophysical Journal 661, L93–L96. doi:10.1086/518719.

Gamborino, D., Vorburger, A., Wurz, P., 2019. Mercury's subsolar sodium exosphere: an ab initio calculation to interpret MASCS/UVVS observations from MESSENGER. Annales Geophysicae 37, 455–470. doi:10.5194/angeo-37-455-2019.

Gershman, D.J., Slavin, J.A., Raines, J.M., Zurbuchen, T.H., Anderson, B.J., Korth, H., Baker, D.N., Solomon, S.C., 2013. Magnetic flux pileup and plasma depletion in Mercury's subsolar magnetosheath. Journal of Geophysical Research: Space Physics 118, 7181–7199. doi:10.1002/2013JA019244.

Glassmeier, K.H., Klimushkin, D., Othmer, C., Mager, P., 2004. ULF waves at Mercury: Earth, the giants, and their little brother compared. Advances in Space Research 33, 1875–1883. doi:10.1016/j.asr.2003.04.047.

Glassmeier, K.H., Mager, P.N., Klimushkin, D., 2003. Concerning ULF pulsations in Mercury's magnetosphere. Geophysical Research Letters 30. doi:10.1029/2003GL017175.

Huebner, W.F., Keady, J.J., Lyon, S.P., 1992. Solar Photo Rates for Planetary Atmospheres and Atmospheric Pollutants. Astrophysics and Space Science 195, 1–294. doi:10.1007/BF00644558.

Huebner, W.F., Mukherjee, J., 2015. Photoionization and photodissociation rates in solar and blackbody radiation fields. Planetary and Space Science 106, 11–45. doi:10.1016/j.pss.2014.11.022.

Hunten, D.M., Morgan, T.H., Shemansky, D.E., 1988. The Mercury atmosphere, in: Vilas, F., Chapman, C.R., Matthews, M.S. (Eds.), Mercury. University of Arizona Press, Tucson, Arizona, USA, pp. 562–612.

James, M.K., Imber, S.M., Yeoman, T.K., Bunce, E.J., 2019. Field Line Resonance in the Hermean Magnetosphere: Structure and Implications for

Plasma Distribution. Journal of Geophysical Research: Space Physics 124, 211–228. doi:10.1029/2018JA025920.

Janches, D., Berezhnoy, A.A., Christou, A.A., Cremonese, G., Hirai, T., Horányi, M., Jasinski, J.M., Sarantos, M., 2021. Meteoroids as One of the Sources for Exosphere Formation on Airless Bodies in the Inner Solar System. Space Science Reviews 217. doi:10.1007/s11214-021-00827-6.

Jasinski, J.M., Cassidy, T.A., Raines, J.M., Milillo, A., Regoli, L.H., Dewey, R., Slavin, J.A., Mangano, V., Murphy, N., 2021. Photoionization Loss of Mercury's Sodium Exosphere: Seasonal Observations by MESSENGER and the THEMIS Telescope. Geophysical Research Letters 48. doi:10.1029/2021GL092980.

Jasinski, J.M., Regoli, L.H., Cassidy, T.A., Dewey, R.M., Raines, J.M., Slavin, J.A., Coates, A.J., Gershman, D.J., Nordheim, T.A., Murphy, N., 2020. A transient enhancement of Mercury's exosphere at extremely high altitudes inferred from pickup ions. Nature Communications 11. doi:10.1038/s41467-020-18220-2.

Jia, X., Slavin, J.A., Gombosi, T.I., Daldorff, L.K.S., Toth, G., Holst, B., 2015. Global MHD simulations of Mercury's magnetosphere with coupled planetary interior: Induction effect of the planetary conducting core on the global interaction. Journal of Geophysical Research (Space Physics) 120, 4763–4775. doi:10.1002/2015JA021143.

Jia, X., Slavin, J.A., Poh, G., DiBraccio, G.A., Toth, G., Chen, Y., Raines, J.M., Gombosi, T.I., 2019. MESSENGER Observations and Global Simulations of Highly Compressed Magnetosphere Events at Mercury. Journal of Geophysical Research (Space Physics) 124, 229–247. doi:10.1029/2018JA026166.

Kallio, E., Chaufray, J.Y., Modolo, R., Snowden, D., Winglee, R., 2011. Modeling of Venus, Mars, and Titan. Space Science Reviews 162, 267–307. doi:10.1007/s11214-011-9814-8.

Killen, R.M., Potter, A.E., Reiff, P., Sarantos, M., Jackson, B.V., Hick, P., Giles, B., 2001. Evidence for space weather at Mercury. Journal of Geophysical Research 106, 20509–20526. doi:10.1029/2000JE001401.

Korth, H., Anderson, B.J., Raines, J.M., Slavin, J.A., Zurbuchen, T.H., Johnson, C.L., et al., 2011. Plasma pressure in Mercury's equatorial magnetosphere derived from MESSENGER Magnetometer observations. Geophysical Research Letters 38. doi:10.1029/2011GL049451.

Korth, H., Johnson, C.L., Philpott, L., Tsyganenko, N.A., Anderson, B.J., 2017. A Dynamic Model of Mercury's Magnetospheric Magnetic Field. Geophysical Research Letters 44, 10,147–10,154. doi:10.1002/2017GL074699.

Korth, H., Tsyganenko, N.A., Johnson, C.L., Philpott, L.C., Anderson, B.J., Al Asad, M.M., Solomon, S.C., McNutt, R.L., 2015. Modular model for Mercury's magnetospheric magnetic field confined within the average observed magnetopause. Journal of Geophysical Research: Space Physics 120, 4503–4518. doi:10.1002/2015JA021022.

Leblanc, F., Chaufray, J.Y., 2011. Mercury and Moon He exospheres: Analysis and modeling. Icarus 216, 551–559. doi:10.1016/j.icarus.2011.09.028.

Leblanc, F., Chaufray, J.Y., Doressoundiram, A., Berthelier, J.J., Mangano, V., López-Ariste, A., Borin, P., 2013. Mercury exosphere. III: Energetic characterization of its sodium component. Icarus 223, 963–974. doi:10.1016/j.icarus.2012.08.025.

Leblanc, F., Chaufray, J.Y., Modolo, R., Leclercq, L., Curry, S., Luhmann, J., et al., 2017a. On the Origins of Mars' Exospheric Nonthermal Oxygen Component as Observed by MAVEN and Modeled by HELIOSARES. Journal of Geophysical Research: Planets 122, 2401–2428. doi:10.1002/2017JE005336.

Leblanc, F., Delcourt, D., Johnson, R.E., 2003. Mercury's sodium exosphere: Magnetospheric ion recycling. Journal of Geophysical Research (Planets) 108. doi:10.1029/2003JE002151.

Leblanc, F., Doressoundiram, A., 2011. Mercury exosphere. II. The sodium/potassium ratio. Icarus 211, 10–20. doi:10.1016/j.icarus.2010.09.004.

Leblanc, F., Doressoundiram, A., Schneider, N., Massetti, S., Wedlund, M., López Ariste, A., et al., 2009. Short-term variations of Mercury's Na exosphere observed with very high spectral resolution. Geophysical Research Letters 36. doi:10.1029/2009GL038089.

Leblanc, F., Johnson, R.E., 2003. Mercury's sodium exosphere. Icarus 164, 261–281. doi:10.1016/S0019-1035(03)00147-7.

Leblanc, F., Johnson, R.E., 2010. Mercury exosphere I. Global circulation model of its sodium component. Icarus 209, 280–300. doi:10.1016/j.icarus.2010.04.020.

Leblanc, F., Oza, A.V., Leclercq, L., Schmidt, C., Cassidy, T., Modolo, R., et al., 2017b. On the orbital variability of Ganymede's atmosphere. Icarus 293, 185–198. doi:10.1016/j.icarus.2017.04.025.

Leclercq, L., Modolo, R., Leblanc, F., Hess, S., Mancini, M., 2016. 3D magnetospheric parallel hybrid multi-grid method applied to planet-plasma interactions. Journal of Computational Physics 309, 295–313. doi:10.1016/j.jcp.2016.01.005.

McClintock, W.E., Bradley, E.T., Vervack, R.J., Killen, R.M., Sprague, A.L., Izenberg, N.R., Solomon, S.C., 2008. Mercury's Exosphere: Observations During MESSENGER's First Mercury Flyby. Science 321, 92. doi:10.1126/science.1159467.

Mcclintock, W.E., Cassidy, T.A., Merkel, A.W., Killen, R.M., Burger, M.H., Vervack, R.J., 2018. Observations of mercury's exosphere: Composition and structure, in: Solomon, S.C., Nittler, L.R., Anderson, B.J. (Eds.), Mercury: The view after MESSENGER. Cambridge Planetary Science, Cambridge. chapter 14, pp. 371–403.

McClintock, W.E., Lankton, M.R., 2007. The Mercury Atmospheric and Surface Composition Spectrometer for the MESSENGER Mission. Space Science Reviews 131, 481–521. doi:10.1007/s11214-007-9264-5.

Merkel, A.W., Cassidy, T.A., Vervack, R.J., McClintock, W.E., Sarantos, M., Burger, M.H., Killen, R.M., 2017. Seasonal variations of Mercury's magnesium dayside exosphere from MESSENGER observations. Icarus 281, 46–54. doi:10.1016/j.icarus.2016.08.032.

Milillo, A., Mangano, V., Massetti, S., Mura, A., Plainaki, C., Alberti, T., Ippolito, A., Ivanovski, S.L., Aronica, A., De Angelis, E., Kazakov, A., Noschese, R., Orsini, S., Rispoli, R., Sordini, R., Vertolli, N., 2021. Exospheric Na distributions along the Mercury orbit with the THEMIS telescope. Icarus 355. doi:10.1016/j.icarus.2020.114179.

Modolo, R., Chanteur, G.M., Wahlund, J.E., Canu, P., Kurth, W.S., Gurnett, D., Matthews, A.P., Bertucci, C., 2007. Plasma environment in the wake of Titan from hybrid simulation: A case study. Geophysical Research Letters 34. doi:10.1029/2007GL030489.

Modolo, R., Hess, S., Mancini, M., Leblanc, F., Chaufray, J.Y., Brain, D., et al., 2016. Mars-solar wind interaction: LatHyS, an improved parallel 3-D multispecies hybrid model. Journal of Geophysical Research (Space Physics) 121, 6378–6399. doi:10.1002/2015JA022324.

Müller, J., Simon, S., Motschmann, U., Schüle, J., Glassmeier, K.H., Pringle, G.J., 2011. A.I.K.E.F.: Adaptive hybrid model for space plasma simulations. Computer Physics Communications 182, 946–966. doi:10.1016/j.cpc.2010.12.033.

Müller, J., Simon, S., Wang, Y.C., Motschmann, U., Heyner, D., Schüle, J., Ip, W.H., Kleindienst, G., Pringle, G.J., 2012. Origin of Mercury's double magnetopause: 3D hybrid simulation study with A.I.K.E.F. Icarus 218, 666–687. doi:10.1016/j.icarus.2011.12.028.

Mura, A., Milillo, A., Orsini, S., Massetti, S., 2007. Numerical and analytical model of Mercury's exosphere: Dependence on surface and external conditions. Planetary and Space Science 55, 1569–1583. doi:10.1016/j.pss.2006.11.028.

Ogilvie, K.W., Scudder, J.D., Hartle, R.E., Siscoe, G.L., Bridge, H.S., Lazarus, A.J., et al., 1974. Observations at Mercury Encounter by the Plasma Science Experiment on Mariner 10. Science 185, 145–151. doi:10.1126/science.185.4146.145.

Orsini, S., Livi, S., Torkar, K., Barabash, S., Milillo, A., Wurz, P., di Lellis, A.M., Kallio, E., SERENA Team, 2010. SERENA: A suite of four instruments (ELENA, STROFIO, PICAM and MIPA) on board BepiColombo-MPO for particle detection in the Hermean environment. Planetary and Space Science 58, 166–181. doi:10.1016/j.pss.2008.09.012.

Orsini, S., Mangano, V., Milillo, A., Plainaki, C., Mura, A., Raines, J.M., De Angelis, E., Rispoli, R., Lazzarotto, F., Aronica, A., 2018. Mercury sodium exospheric emission as a proxy for solar perturbations transit. Scientific Reports 8. doi:10.1038/s41598-018-19163-x.

Oza, A.V., Leblanc, F., Johnson, R.E., Schmidt, C., Leclercq, L., Cassidy, T.A., Chaufray, J.Y., 2019. Dusk over dawn O$_2$ asymmetry in Europa's near-surface atmosphere. Planetary and Space Science 167, 23–32. doi:10.1016/j.pss.2019.01.006.

Paral, J., Trávníček, P.M., Rankin, R., Schriver, D., 2010. Sodium ion exosphere of Mercury during MESSENGER flybys. Geophysical Research Letters 37. doi:10.1029/2010GL044413.

Potter, A.E., Killen, R.M., Reardon, K.P., Bida, T.A., 2013. Observation of neutral sodium above Mercury during the transit of November 8, 2006. Icarus 226, 172–185. doi:10.1016/j.icarus.2013.05.029.

Potter, A.E., Killen, R.M., Sarantos, M., 2006. Spatial distribution of sodium on Mercury. Icarus 181, 1–12. doi:10.1016/j.icarus.2005.10.026.

Potter, A.E., Morgan, T.H., 1985. Discovery of Sodium in the Atmosphere of Mercury. Science 229, 651–653. doi:10.1126/science.229.4714.651.

Potter, A.E., Morgan, T.H., 1986. Potassium in the atmosphere of Mercury. Icarus 67, 336–340. doi:10.1016/0019-1035(86)90113-2.

Raines, J.M., DiBraccio, G.A., Cassidy, T.A., Delcourt, D.C., Fujimoto, M., Jia, X., Mangano, V., Milillo, A., Sarantos, M., Slavin, J.A., Wurz, P., 2015. Plasma Sources in Planetary Magnetospheres: Mercury. Space Science Reviews 192, 91–144. doi:10.1007/s11214-015-0193-4.

Raines, J.M., Gershman, D.J., Slavin, J.A., Zurbuchen, T.H., Korth, H., Anderson, B.J., Solomon, S.C., 2014. Structure and dynamics of Mercury's magnetospheric cusp: MESSENGER measurements of protons and planetary ions. Journal of Geophysical Research: Space Physics 119, 6587–6602. doi:10.1002/2014JA020120.

Raines, J.M., Gershman, D.J., Zurbuchen, T.H., Sarantos, M., Slavin, J.A., Gilbert, J.A., et al., 2013. Distribution and compositional variations of plasma ions in Mercury's space environment: The first three Mercury years of MESSENGER observations. Journal of Geophysical Research: Space Physics 118, 1604–1619. doi:10.1029/2012JA018073.

Raines, J.M., Wallace, K.L., Sarantos, M., Jasinksi, J.M., Tracy, P.J., Dewey, R.M., et al., 2018. First In-Situ Observations of Exospheric Response to CME Impact at Mercury, in: Mercury: Current and Future Science of the Innermost Planet, Proceedings of the conference held 1-3 May, 2018 in Columbia, Maryland.

Richer, E., Modolo, R., Chanteur, G.M., Hess, S., Leblanc, F., 2012. A global hybrid model for Mercury's interaction with the solar wind: Case study of the dipole representation. Journal of Geophysical Research (Space Physics) 117. doi:10.1029/2012JA017898.

Romanelli, N., Modolo, R., Leblanc, F., Chaufray, J.Y., Hess, S., Brain, D., Connerney, J., et al., 2018a. Effects of the Crustal Magnetic Fields and Changes in the IMF Orientation on the Magnetosphere of Mars: MAVEN Observations and LatHyS Results. Journal of Geophysical Research (Space Physics) 123, 5315–5333. doi:10.1029/2017JA025155.

Romanelli, N., Modolo, R., Leblanc, F., Chaufray, J.Y., Martinez, A., Ma, Y., et al., 2018b. Responses of the Martian Magnetosphere to an Interplanetary Coronal Mass Ejection: MAVEN Observations and LatHyS Results. Geophysical Research Letters 45, 7891–7900. doi:10.1029/2018GL077714.

Saito, Y., Sauvaud, J.A., Hirahara, M., Barabash, S., Delcourt, D., Takashima, T., Asamura, K., BepiColombo MMO/MPPE Team, 2010. Scientific objectives and instrumentation of Mercury Plasma Particle Experiment (MPPE) onboard MMO. Planetary and Space Science 58, 182–200. doi:10.1016/j.pss.2008.06.003.

Sarantos, M., Killen, R.M., Kim, D., 2007. Predicting the long-term solar wind ion-sputtering source at Mercury. Planetary and Space Science 55, 1584–1595. doi:10.1016/j.pss.2006.10.011.

Sarantos, M., Slavin, J.A., Benna, M., Boardsen, S.A., Killen, R.M., Schriver, D., Trávníček, P., 2009. Sodium-ion pickup observed above the magnetopause during MESSENGER's first Mercury flyby: Constraints on neutral exospheric models. Geophysical Research Letters 36. doi:10.1029/2008GL036207.

Schmidt, C.A., 2013. Monte Carlo modeling of north-south asymmetries in Mercury's sodium exosphere. Journal of Geophysical Research (Space Physics) 118, 4564–4571. doi:10.1002/jgra.50396.

Seki, K., Terada, N., Yagi, M., Delcourt, D.C., Leblanc, F., Ogino, T., 2013. Effects of the surface conductivity and the IMF strength on the dynamics of planetary ions in Mercury's magnetosphere. Journal of Geophysical Research (Space Physics) 118, 3233–3242. doi:10.1002/jgra.50181.

Shue, J.H., Chao, J.K., Fu, H.C., Russell, C.T., Song, P., Khurana, K.K., Singer, H.J., 1997. A new functional form to study the solar wind control of the magnetopause size and shape. Journal of Geophysical Research 102, 9497–9512. doi:10.1029/97JA00196.

Siscoe, G.L., Ness, N.F., Yeates, C.M., 1975. Substorms on Mercury? Journal of Geophysical Research 80, 4359. doi:10.1029/JA080i031p04359.

Slavin, J.A., Acuña, M.H., Anderson, B.J., Baker, D.N., Benna, M., Boardsen, S.A., Gloeckler, G., Gold, R.E., Ho, G.C., Korth, H., Krimigis, S.M., McNutt, R.L., Raines, J.M., Sarantos, M., Schriver, D., Solomon, S.C., Trávníček, P., Zurbuchen, T.H., 2009. MESSENGER Observations of Magnetic Reconnection in Mercury's Magnetosphere. Science 324, 606. doi:10.1126/science.1172011.

Slavin, J.A., Acuña, M.H., Anderson, B.J., Baker, D.N., Benna, M., Gloeckler, G., et al., 2008. Mercury's Magnetosphere After MESSENGER's

840   First Flyby. Science 321, 85. doi:10.1126/science.1159040.

841   Slavin, J.A., DiBraccio, G.A., Gershman, D.J., Imber, S.M., Poh, G., Raines, J.M., Zurbuchen, T.H., Jia, X., Baker, D.N., Glassmeier, K.H., Livi,
842   S.A., Boardsen, S.A., Cassidy, T.A., Sarantos, M., Sundberg, T., Masters, A., Johnson, C.L., Winslow, R.M., Anderson, B.J., Korth, H., McNutt,
843   R.L., Solomon, S.C., 2014. MESSENGER observations of Mercury's dayside magnetosphere under extreme solar wind conditions. Journal of
844   Geophysical Research: Space Physics 119, 8087–8116. doi:10.1002/2014JA020319.

845   Slavin, J.A., Krimigis, S.M., Acuña, M.H., Anderson, B.J., Baker, D.N., Koehn, P.L., Korth, H., Livi, S., Mauk, B.H., Solomon, S.C., Zurbuchen,
846   T.H., 2007. MESSENGER: Exploring Mercury's Magnetosphere. Space Science Reviews 131, 133–160. doi:10.1007/s11214-007-9154-x.

847   Slavin, J.A., Middleton, H.R., Raines, J.M., Jia, X., Zhong, J., Sun, W.J., Livi, S., Imber, S.M., Poh, G.K., Akhavan-Tafti, M., Jasinski, J.Â.M.,
848   DiBraccio, G.A., Dong, C., Dewey, R.M., Mays, M.L., 2019. MESSENGER Observations of Disappearing Dayside Magnetosphere Events at
849   Mercury. Journal of Geophysical Research: Space Physics 124, 6613–6635. doi:10.1029/2019JA026892.

850   Smith, D.E., Zuber, M.T., Phillips, R.J., Solomon, S.C., Hauck, S.A., Lemoine, F.G., Mazarico, E., Neumann, G.A., Peale, S.J., Margot, J.L.,
851   Johnson, C.L., Torrence, M.H., Perry, M.E., Rowlands, D.D., Goossens, S., Head, J.W., Taylor, A.H., 2012. Gravity Field and Internal Structure
852   of Mercury from MESSENGER. Science 336, 214. doi:10.1126/science.1218809.

853   Smyth, W.H., Marconi, M.L., 1995. Theoretical Overview and Modeling of the Sodium and Potassium Atmospheres of Mercury. The Astrophysical
854   Journal 441, 839. doi:10.1086/175407.

855   Soter, S., Ulrichs, J., 1967. Rotation and Heating of the Planet Mercury. Nature 214, 1315–1316. doi:10.1038/2141315a0.

856   Turc, L., Leclercq, L., Leblanc, F., Modolo, R., Chaufray, J.Y., 2014. Modelling Ganymede's neutral environment: A 3D test-particle simulation.
857   Icarus 229, 157–169. doi:10.1016/j.icarus.2013.11.005.

858   Vervack, R.J., Killen, R.M., McClintock, W.E., Merkel, A.W., Burger, M.H., Cassidy, T.A., Sarantos, M., 2016. New discoveries from MESSEN-
859   GER and insights into Mercury's exosphere. Geophysical Research Letters 43, 11,545–11,551. doi:10.1002/2016GL071284.

860   Winslow, R.M., Anderson, B.J., Johnson, C.L., Slavin, J.A., Korth, H., Purucker, M.E., Baker, D.N., Solomon, S.v., 2013. Mercury's magnetopause
861   and bow shock from MESSENGER Magnetometer observations. Journal of Geophysical Research: Space Physics 118, 2213–2227. doi:10.
862   1002/jgra.50237.

863   Winslow, R.M., Johnson, C.L., Anderson, B.J., Korth, H., Slavin, J.A., Purucker, M.E., Solomon, S.C., 2012. Observations of Mercury's northern
864   cusp region with MESSENGER's Magnetometer. Geophysical Research Letters 39. doi:10.1029/2012GL051472.

865   Winslow, R.M., Lugaz, N., Philpott, L., Farrugia, C.J., Johnson, C.L., Anderson, B.J., Paty, C.S., Schwadron, N.A., Asad, M., 2020. Observations
866   of Extreme ICME Ram Pressure Compressing Mercury's Dayside Magnetosphere to the Surface. The Astrophysical Journal 889. doi:10.3847/
867   1538-4357/ab6170.

868   Wurz, P., Lammer, H., 2003. Monte-Carlo simulation of Mercury's exosphere. Icarus 164, 1–13. doi:10.1016/S0019-1035(03)00123-4.

869   Yagi, M., Seki, K., Matsumoto, Y., Delcourt, D.C., Leblanc, F., 2010. Formation of a sodium ring in Mercury's magnetosphere. Journal of
870   Geophysical Research (Space Physics) 115. doi:10.1029/2009JA015226.

871   Yagi, M., Seki, K., Matsumoto, Y., Delcourt, D.C., Leblanc, F., 2017. Global Structure and Sodium Ion Dynamics in Mercury's Magnetosphere
872   With the Offset Dipole. Journal of Geophysical Research (Space Physics) 122, 10,990–11,002. doi:10.1002/2017JA024082.

873   Zurbuchen, T.H., Raines, J.M., Gloeckler, G., Krimigis, S.M., Slavin, J.A., Koehn, P.L., et al., 2008. MESSENGER Observations of the Composition
874   of Mercury's Ionized Exosphere and Plasma Environment. Science 321, 90. doi:10.1126/science.1159314.

875   Zurbuchen, T.H., Raines, J.M., Slavin, J.A., Gershman, D.J., Gilbert, J.A., Gloeckler, G., Anderson, B.J., Baker, D.N., Korth, H., Krimigis, S.M.,
876   Sarantos, M., Schriver, D., McNutt, R.L., Solomon, S.C., 2011. MESSENGER Observations of the Spatial Distribution of Planetary Ions Near
877   Mercury. Science 333, 1862. doi:10.1126/science.1211302.